Use of Photometric Stereo for the Accurate Modelling of Three-Dimensional Skin Microrelief

Ali Sohaib

A thesis submitted in partial fulfilment of the requirements of the University of the West of England, Bristol for the degree of Doctor of Philosophy

Faculty of the Environment and Technology

University of the West of England, Bristol

October 2013

Abstract

The largest organ of human body - ”skin” is a multilayered organ with complex reflectance properties that not only vary with the direction of illumination but also with the wavelength of light. The complex Three Dimensional (3D) structure and optical properties of human skin makes it very difficult for techniques like Photometric stereo to accurately recover its 3D shape. One problem in particular concerns the presence of interreflections at concave regions of the skin surface topography. Common features such as wrinkles, moles, lesions, burns and surgical scars can appear as elevated skin area or as indentations in the skin surface, and usually have a different colour when compared to the surrounding skin. These differences in colour and the degree of concavity determine the amount of interreflection present and hence significantly affect the overall recovery of the 3D topography of the skin. This thesis explores the use of varying incident light wavelength in the visible spectrum to improve the recovered topography of human skin. New algorithms were developed and implemented to minimise the effects of interreflections and an accuracy assessment of using wavelengths in the visible spectrum was carried out for Caucasian, Asian and African American skin types. The results demonstrate that white light is not ideal for imaging skin relief and also illustrate the differences in recovered skin topography due to a non-diffuse Bidirectional Reflectance Distribution Function (BRDF) for each colour illumination used.

In addition to the complication caused by interreflections, the translucency of skin allows light to scatter within the skin. This confutes the assumption associated with photometric stereo that - light incident on a particular patch of the skin is reflected at the same point. This issue is taken care of by incorporating polarisation information with photometric stereo to improve the 3D skin shape recovery. The experiments conducted show improvement in the recovered skin

topography when specular reflected light was used instead of the multiply sub-surface scattered diffuse light emanating from within the skin. The results also show an increase in polarised reflected light as the albedo of the skin decreases with wavelength in the visible spectrum, while darker skin tend to reflect more polarised light than lighter skin at similar wavelengths in the visible spectrum. These characteristics of human skin have not been investigated before and are important additions to the current state of the art in skin optics.

Acknowledgements

This research project would not have been possible without the support of many people. Foremost, I would like to express my gratitude to my principal supervisor Professor Melvyn Smith for his support and thoughtful guidance during my Ph.D study. In addition, I would like to acknowledge my supervisory team Dr Lyndon Smith, Dr Abdul Farooq and Mr Robb Warr for their invaluable assistance in the completion of this thesis and for providing constructive feedback on my research throughout.

I would also like to express my gartitude to Dr Jeffrey Bamber and Nigel Bush at the Institute of Cancer Research, Sutton, UK for allowing me to use the PRIMOS device. Furthermore, I would like to take this opportunity to thank all my colleagues at the Centre for Machine Vision, UWE, especially Laurence Broadbent for his help with the CAD drawings of the numerous parts made during my PhD and Jahanzeb Ahmed for his help with the PovRay software. I would also like to thank Christopher Hart for the rapid prototyping of various parts used in the experiments.

I am also thankful to all the participants who agreed to take part in this research study.

Finally, I would like to express my deepest gratitude to my family: Mum, Dad, my brother and sister and my wife for their endless patience, support and encouragement when it was most required.

This work is dedicated to my family, especially Mum and Dad.

Contents

List of Figures

List of Publications Arising from this Work

Journal Publications

[1] A. Sohaib, A. R. Farooq, G. A. Atkinson, L. N. Smith, M. L. Smith and R. P. Warr “In vivo Measurement of skin microrelief using photometric stereo in the presence of interreflections,” Journal of the Optical Society of America A, vol. 30, no. 3, Mar. 2013.[Published]

[2] A. Sohaib, A. R. Farooq, L. N. Smith, and M. L. Smith, “Shape from Specular reflection using Polarisation,” Journal of Modern Optics, [to be submitted]

[3] A. Sohaib, A. R. Farooq, L. N. Smith, M. L. Smith, J. Paget and R. P. Warr, “Quantification and objective evaluation of wrinkles,” Dermatologic Surgery, [to be submitted]

Conference and posters

[1] Ali Sohaib, Abdul R. Farooq, Lyndon N. Smith, Melvyn L. Smith and Robert Warr: ”3D In-Vivo Measurement of Skin Topography Using Photometric Stereo”, in Proc. International conference on 3D Body scanning Technologies, Lugano, Switzerland, pp. 21-29, 2012.

[2] Ali Sohaib, Abdul R. Farooq, Lyndon N. Smith, Melvyn L. Smith, ” Accurate Recovery of Skin Microrelief Using Photometric Stereo ”, British Machine Vision Association (BMVA) Manchester July 2011, (Poster presentation).

[3] Ali Sohaib, Abdul R. Farooq, Lyndon N. Smith, Melvyn L. Smith, ”Quantification of Wrinkles Using Photometric Stereo”, Bristol-Cardiff young vision researchers’ colloquium, Bristol, July 2011, (Poster presentation)

Chapter 1

Introduction

Human skin is a multilayered organ with complex optical and physical properties. It is translucent - meaning that light can penetrate through skin, get scattered, transmitted or absorbed and part of it ultimately comes out of the skin. Many conventional photometric analysis methods such as shape from shading and photometric stereo become difficult to implement in the presence of interreflections and subsurface scattering. It is well known that the main reasons that these methods are limited is because of unrealistic assumptions made about the optical properties of the surface, e.g. having a Lambertian (diffuse reflection) BRDF. Although there is evidence of research undertaken to tackle noise from shadows and interreflections [2–4], there is little work concerning the modeling of sub-surface scattering and interreflections in human skin when using photometric stereo. This is particularly relevant when examining the surface of human skin due to its mixed

mode reflection properties.

Diffusely reflected light has been considered to be a positive characteristic for surfaces that are analysed using a photometric stereo technique, as they fit better to the Lambertian assumption associated with conventional photometric stereo. However diffuse light reflection model is beneficial only for opaque and non-concave surfaces. Skin on the other hand is translucent and the diffusely reflected light contains additional noise(subsurface scattering + interreflections) compared to specularly reflected light. To encapsulate on the relationship between subsurface reflection and skin, the light reflection from the skin can be defined by models such as the BSSRDF (bidirectional surface scattering reflectance distribution function), however they are very expensive to capture and their incorporation in photometric stereo is not possible as the parameters of the BSSRDF model cannot be extracted from photometric stereo data alone. This thesis looks at alternative techniques like 'polarimetric photometric stereo' to separate the subsurface diffusely scattered light from specularly reflected light. The idea of using only the specularly reflected light will be explored in some detail, as it provides a usefully inexpensive and computationally efficient way of recovering the 3D relief of skin by overcoming the inaccuracies in recovered topography added due to the presence of subsurface scattered light.

This new form of photometric stereo allows the acquisition and recovery of both reflectance and 3D topography data and despite the human skin complex surface texture, Photometric Stereo is ideally suited to recovering this type of dense surface texture. Moreover, clinical input has identified a need for objectifying the measurement of skin texture, in both cosmetic and clinical applications. Therefore, the development of a measure for quantifying the skin microrelief is essential. This has wide ranging applications for being able to assess skin pre and post medical interventions or in cosmetic skin rejuvenation methods.

1.1 Original Contributions

The major original contributions of the work presented in this thesis are:

- The finding that the BRDF of skin varies with wavelength in the visible spectrum and that it also varies with different skin types.
- The development and implementation of a novel photometric stereo technique that is able to mitigate the effects of interreflection for the in-vivo analysis of human skin, for different skin types where there is a difference in reflectance for each skin type as well as a difference in BRDF.
- To the best of author's knowledge, no published work has so far looked

into the quantitative assessment of 3D skin microrelief using photometric stereo. Much of the analysis concerning the accuracy of skin microrelief is visually qualitative. The skin topography measurements presented in this thesis were validated using the PRIMOS 4 device and detailed experiments were performed with different skin types to determine the amount of error in surface normals and reconstructed height for each individual colour (R, G, B) and white light caused by differences in BRDF.

- Earlier work regarding the surface accuracy analysis between infrared and white light showed that infrared was superior in capturing accurate skin topography to white light [5]. This thesis further contributes to the state-of the-art by explaining the reasons for inaccurate acquisition of skin topography while using white light.

- The development of a new technique for minimizing surface errors due to interreflection in the presence of wrinkles. (Using variation in spectral gradients)

- An algorithm for interreflection minimisation using segmentation based method.

- The finding that human skin reflects more polarised light as the reflectance decreases (in visible spectrum) and darker skin exhibits a higher degree of

polarisation than lighter skin at similar wavelengths in the visible spectrum. (The Umov effect for skin).

- A novel algorithm for shape from specular reflection using polarimetric photometric stereo (Verified using simulated and real data).

1.2 Applications of Research

The presence of scars, wrinkles and uneven pigmentation in skin can be aesthetically distressing, and can lead to functional and psychological problems for individuals. Therefore there is a need for accurate measurements of these conditions in order to quantify improvement and assess the efficacy of remedial procedures. According to a survey, every year around 100 million patients acquire scars as a result of surgical procedures, trauma, facial plastic and reconstructive surgery [6]. Moreover, the numbers for keloidal scars and burn scars are estimated to be in range of 11 million and 4 million respectively, with the majority occurring in children.

In case of wrinkles the cost of minimally invasive cosmetic procedures has grown annually in the USA from 5.5 million dollars in 2000 to 10.4 million dollars in 2008. A further breakdown reveals the extent of the demand for the treatment

of wrinkles; this includes 5,014,446 Botox procedures, 400,262 laser resurfacing procedures and 1,593,632 uses of soft tissue fillers [7]. A similar trend is seen in the market for cosmetic products in Europe with facial products making up 59.3% of a 23.4 billion dollar market with an average annual growth of 3.7% since 2005 [8].

There exist a multitude of subjective and qualitative scales for analysis of scars and wounds, however the need for more objective analysis requires an ability to record fine 3D facial morphology in order to measure and calculate changes in topography, volumetric changes, texture and skin tone. Similarly in the case of wrinkles there exists a lack of standardised efficacy evaluation techniques, which in turn makes any subsequent treatment and analysis qualitative and subjective [9]. Although the widespread demand and burgeoning number of treatments on offer has also seen a corresponding increase in the process of classification of wrinkles in an attempt to stratify the process and therefore guide treatment, there does not appear to be, as yet, a definitive wrinkle classification system based on an objective series of measurements.

This thesis investigates the relevant anatomy and optical properties of human skin and reviews current 3D imaging systems for the development of a system able to capture the fine topography of human skin. Also included is a comparison of the

current classification methods in order to determine the necessary characteristics of a wrinkle classification system and a subsequent discussion of the potential for using novel 3D imaging systems that could be used in a clinical setting.

1.3 Thesis Outline

The literature review in the following chapter aims to provide the context of this work from an application point of view. 3D imaging techniques are next reviewed, followed by an overview of current scar and wrinkle grading systems and current standards for efficacy assessment for treatments.

An introduction to photometric stereo is provided in Chapter 3. Also provided is a discussion of existing reflectance models available for modelling light interaction with surfaces. The parameters for reflectance models such as Lambertian, Phong, blinn-Phong, Ward, Oren Nayer and Torrance Sparrow are individually discussed, as some of these models will be further used in chapter 5 for detailed analysis .

Chapter 4 leads into the problem of interreflection by examining the literature concerning the optics of human skin and how it varies for different skin types at various wavelengths in the visible spectrum and its effects on interreflected light. The chapter also explains the validation of the recovered topography obtained by

photometric stereo by using PRIMOS data as ground truth. The results show that the BRDF of skin varies with wavelength in the visible spectrum and that red light is more suitable for 3D shape recovery than using either green or blue light. A novel algorithm based on segmentation of interreflected areas in skin is presented followed by an improved algorithm based on a gradient spread technique.

Chapter 5 discusses and presents a novel method for incorporating a Torrance and Sparrow model of light reflection with photometric stereo to improve the 3D shape recovery of skin. The problem of interreflected and subsurface scattered light causes loss of high frequency information of skin relief, by separating the specular and diffuse components of light using polarisers the high frequency surface information can be recovered by using a novel algorithm that uses specular reflected light only. Also presented is the experimental analysis of the Umov effect for skin which shows a variation in degree of polarisation of light for Caucasian and Asian skin types.

In Chapter 6 there is a discussion of the major original contributions presented in this thesis and the limitations of proposed techniques. Finally there is a section which explores some future extensions of this work and how the techniques presented can be extended generally to more complex problems.

Chapter 2

Literature survey

2.1 Review of Wrinkle Grading Scales

Visible wrinkles and skin relief are a result of the three dimensional structural organisation of the dermis and subcutaneous tissue. This complex composition is affected by both physiological and environmental factors. Increased demand for treatment of wrinkles has led to a proliferation of different pharmaceutical and surgical treatment methods. However there still remains a lack of quantitative, objective, easily utilisable and reproducible classifications of wrinkles by which these treatments can be studied and compared.

With ever increasing pressures to appear youthful there has been a huge growth in the demand for effective treatments of wrinkles. There are now a wide

variety of treatments on offer ranging from ”over the counter” pharmaceutical creams to minor surgical procedures, alternative medical therapies to invasive cosmetic surgery. This demand is increasing; for example, the number of minimally invasive cosmetic procedures has grown annually in the USA from 5.5 million in 2000 to 10.4 million in 2008. Further breakdown reveals the extent of the demand in the treatment of wrinkles, with 5,014,446 botox procedures, 400,262 laser resurfacing procedures and 1,593,632 uses of soft tissue fillers [7]. A similar trend is seen in the market for cosmetic products in Europe with facial products making up 59.3% of a 23.4 billion dollar market with an average annual growth of 3.7% since 2005 [8].

The next sections present a short review of the relevant anatomy and optical properties of the skin and a review of 3D imaging systems. This is followed by comparison of the current classification methods in order to determine the necessary characteristics of a wrinkle classification system and the potential for using novel 3D imaging systems for use in clinical settings.

2.2 Skin Anatomy

Skin has a multilayer structure comprising epidermis, derived embryologically from ectoderm, dermis from mesoderm and subcuticular fat as shown in Fig.

2.1(a). It also contains a number of epidermal appendages - for example hair cells and both eccrine and apocrine sweat glands that exist across different layers and originate from the ectoderm. At a more detailed level, the histology of the stratified squamous epithelial epidermis comprises the different stages of keratinocytes maturation (from the outside in), a horny cell layer = stratum corneum, a granular layer named for the keratohyalin granules within the cells, a pigmented prickle cell layer and a basal layer shown in Fig. 2.1(b). The basal cells are anchored at their lower edge to the basement membrane, itself a tight layer separating the dermis and epidermis. Langerhans cells (comprising part of the immune system) exist in the prickle cell layer. Melanocytes (which contain the melanin pigment producing melanosomes) vary with skin type: concentrated in melanosomal groups in ”white” skin and more evenly distributed throughout the epidermis in ”black” skin. The basement membrane is attached by keratin filaments of hemidesmosomes to the basal cell layer keratinocytes. It is itself comprised of three layers (from outer to inner): lamina lucida, lamina densa and sublamina densa. The lamina densa, comprising type IV collagen and laminis, is the principal layer for anchoring receiving the lower anchoring keratins from hemidesmosomes above and being anchored itself via anchoring fibrils (type VII collagen) to the collagen of the dermis below.

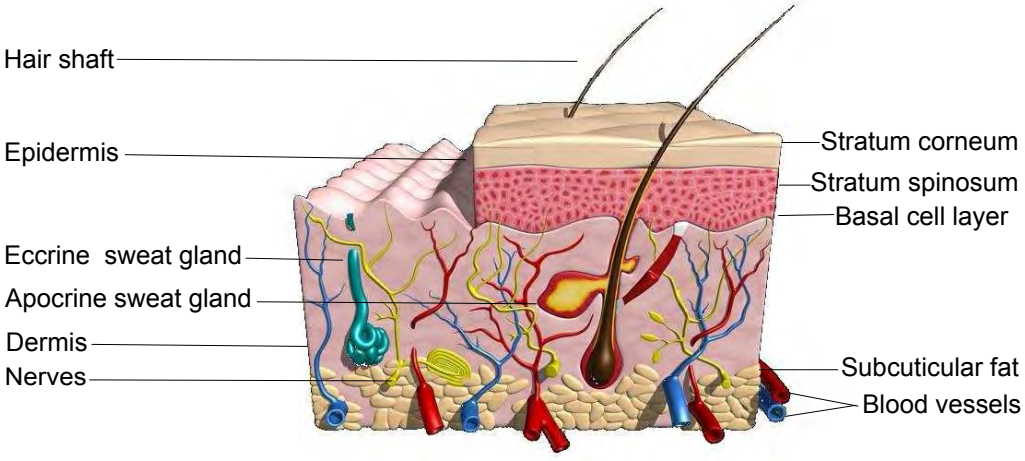

(a)

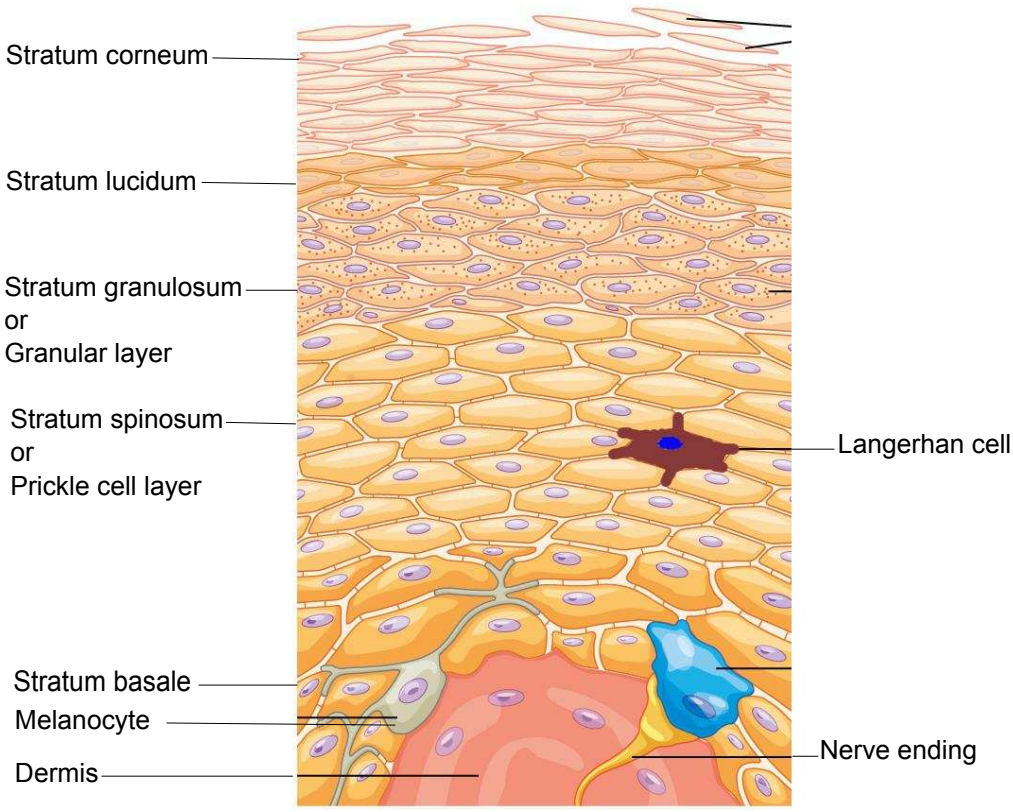

(b)

Figure 2.1: (a) Cross-sectional view of skin showing epidermis, dermis and appendage structures. (b) Cellular structure of epidermis

The dermis is comprised mostly of connective tissue. The dermis and epidermis interdigitate via downwards epiderma rete ridges and upwards dermal papillae. Underneath this interface and anchored to it, as described above, is a network of collagen and elastin embedded in mucopolysaccharides with thinner bundles of fibres in the upper dermis and thicker bundles of fibres in the lower dermis. It also contains a number of specialized cells: macrophages and mast cells (both involved with immune responses) and fibroblasts (which among other roles produce the connective tissue proteins collagen and elastin).

The skin's blood supply runs in an upward projection of capillaries from a plexus in the subcuticular fat layer to a further network within the dermis. The dermis has a higher hemoglobin oxygen saturation than the epidermis by up to an order of magnitude. Seen under a high power microscope, skin is not smooth. Both the very surface of the keratinocytes and the underlying epidermis and dermis contribute to the microtopography.

Hashimoto [10] classified skin surface topographic structure into four categories; primary, secondary, tertiary and quaternary lines using SEM (Scanning electron microscope) images. The primary lines consist of deep lines or furrows which divide the skin into small mesh like structures, made up of numerous triangles and other polygonal shapes. The secondary lines cross over the layer of horny

cells and connect adjacent primary lines, these are much shorter in length and less deeper than the primary lines. The other two structures are formed by a layer of dead cells called horny cells which make up the topmost layer of Stratum corneum. The boundary of these cells forms the tertiary structure and the lines on surface of individual horny cells forms the quaternary structure. These two structures are responsible for the diffuse reflection of light from the skin surface [11].

Only the primary and secondary structures are studied for the evaluation of skin treatment efficacy and roughness measurements and these are in depth ranges of 20μm-100μm and 5μm-40μm respectively [12].

2.3 Optical Properties of Skin

In general, surfaces exhibit three main types of light interaction, these are absorption, transmission and reflection as shown in Fig. 2.2. Material atomic structure and incident light properties dictate the type of interaction exhibited by a particular material. The composition of white light is a mixture of wavelengths of the visible electromagnetic spectrum. Light falling on a surface is selectively absorbed, transmitted and reflected, where this behaviour is dependent on the ma-

terial properties. Absorption occurs when the natural resonating frequency of the electrons in the material matches that of the incident radiation. The light energy is subsequently converted into heat energy due to the hugely intensified vibrations. Transmission of light is observed when the incident radiation frequency does not match the natural frequency of a transparent material. There is a limited impact on the natural vibrations of the electrons and therefore there is no significant change of energy state but through the transfer of electron and atom vibrations the light is allowed to pass through the material. Refraction can be considered as a subset of transmission, where the passage of light energy is slowed by the material, thus bending the light at the interfaces of the material(s). For an opaque

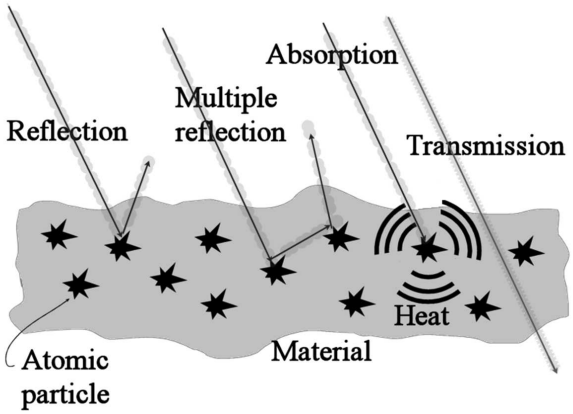

Figure 2.2: Interaction of light with skin.

material and again where the natural frequency does not match that of the incident electromagnetic energy, the light is not transferred electron to electron but is effectively rejected near to the point of entry. This phenomenon is known as

reflection. Particular combinations of absorption, transmission and reflection give rise to the colour and textural characteristics of a surface. For example, the absorption of certain dominant wavelengths of light results in the surface radiating a specific colour.

The outer layers of skin are not opaque. What we see is a composition of the effect that both the microtopography of the surface as well as its underlying constituents have. Inherently skin can absorb and scatter light (part of the later leading to the measured reflectance). Measuring the absorption coefficient and the scattering coefficient as well as the chromophore (light absorbing pigments) concentrations of skin have been used in different aesthetic, diagnostic and therapeutic applications from detection of cancer with fluorescence [13] to photodynamic therapy [14].

However the measurement of these properties is difficult to interpret as the skin's underlying anatomy and physiology influence them: for example the microscopic structure of the surface keratinocytes is similar enough to the wavelength of light to cause diffraction and the relative concentrations of chromophores affect the absorption of light (hemoglobin absorbs strongly at wavelengths around 600nm, water at 980nm and various other skin pigments at other wavelengths. The overall absorption effect has been seen to vary depending on anatomical location and

local physiology e.g. temporary venous obstruction [15].

Absorption is also seen to be coupled to scattering with more absorption leading to less scattering. Scatter itself is influenced by the interaction between the surface anatomy and light as well as the results of the interactions between light and the underlying structures of skin.

Determining the underlying contribution of the resulting reflectance (i.e. return of light) from skin is therefore a complex subject with many models proposed for untangling the underlying contributions of the different components [16–18].

In trying to objectively analyse wrinkles, we are interested in the shape of the skin at the surface - its micro topography. Imaging this in any form has to account for the complex interactions of light with the skin.

2.4 Wrinkle Grading

In the absence of an objective 2D or 3D evaluation technique, clinicians make use of wrinkle grading scales for assessing the efficacy of different treatments. These scales can be categorised into three types i.e. descriptive, visual analogue and photographic scales. Most of these scales are designed for specific body regions like cheek sagging [19], crow feet [19], nasolabial folds [20], lip fullness/wrinkles [21, 22], marionette lines [23], and the forehead [24], while a few are intended for

the entire face [25, 26]. The majority of the grading scales are limited in scope; some are only suitable for measurement of treatment outcome [27], while some are suitable for analysis of photodamage only [26, 28], or skin ageing. There is currently no universal scale available which covers all mentioned analysis and also accounts for all ethnic groups and gender.

Only photographic scales are discussed in the next section as they are more frequently used over other grading scales and they have also proven to be superior to other grading scales [29, 30].

2.4.1 Photographic Scales

This type of grading scale is usually a subgroup of photographs taken from a pool of pictures [26] and thus cannot represent minor changes in wrinkle intensities. If a wrinkle lies in between any two grades, it will likely be assigned to one of a higher or lower wrinkle intensity position hence producing an inaccurate assessment. However by using 3D imaging this error can be minimised.

The modified Fitzpatrick scale [31] represents increasing wrinkle severity in terms of a photographic scale, also added is a description of each interval. Day's 5-point wrinkle severity rating scale (WSRS) [9] shows similarity to the modified Fitzpatrick scale as both are photographic scales with descriptions. The Fitzpatrick

scale provides more intervals for classification, however adding more intervals has been shown to have no effect on improving the assessment as the intra-observer assessment was found to be similar to the 5-point WSRS [31].

The ageing process is quite complicated and it is a function of a number of variables such as wrinkle severity, smoking, pigmentation, gender, sun-hours (UV exposure), ethnicity and oxidative stress due to long term exposure to air pollution [32]. Its clinical signs not only take the form of wrinkles but also colour, translucency, lentigines and skin turgor. So a mere descriptive or photo-numeric wrinkle scale alone is not enough for assessment of the skin ageing process. Glogau classification also takes skin colour into account, however it does not attend to a specific wrinkle type or particular area of the face [33]. Lemperle provided a comprehensive photographic scale for specific regions of the face and neck. The scale consists of 5 levels of varying wrinkle severity over 12 different regions on the face and neck.

The photoageing phenomenon also alters the skin microstructure hence cannot be classified using photographic scales by the examiner. Wrinkles are thought to be prominent features of photoageing, however it is more common in Caucasian skin rather than Asian skin where changes in pigmentation are more noticeable and changes in wrinkles become prominent at a later age [28]. Hence wrinkle

severity does not necessarily need to draw a parallel with pigmentary changes [26] and cannot alone be used for analysis of photodamage.

Chung et. al. [28] devised 8-point and 6-point photographic scales for assessment of wrinkles and dyspigmentation for both sexes. When the scales were interchangeably used for men and women there was disagreement within 1 grade for 32% of the women and 22% of the men graded. This demonstrated that contrary to common belief, dyspigmentation is a prominent feature in photoageing not wrinkling when considering Asian skin.

Unlike the majority of wrinkle grading systems, the Beagley-Gibson system is intended for classification of skin microtopography. It uses a 6 point scale with standard photographs and descriptions of each scale describing changing primary and secondary line structures in terms of depth, distortion and loss of lines. This scale has been used to study changes in skin microtopography due to ultraviolet exposure [33, 34] however the analysis with this system is subjective and it is difficult to differentiate minor differences in skin microrelief using visual assessment.

2.4.2 Conditions for Analysis

Open and closed eyelids can affect wrinkle intensities assessment around forehead, crowpad, upper and lower eye lids and glabellar lines with prominent differences among ethnic groups and age [35].

It is important that during assessment using these scales the lighting conditions are kept the same because the skin can appear to be different under changing lighting conditions. This also applies to viewing photographs when they are presented to the clinician for analysing.

Development and use of photographic scales does require care and special equipment for setting up optimal lighting conditions for the acquisition of high quality photographs [26].

2.4.3 Wrinkle Grading Systems Discussion

The use of photographic scales for evaluation are more promising than the use of descriptive scale. However their suitability for analysis depends on their intended use; some of these grading systems are only suitable for analysis of a single parameter of treatment outcome, such as improvement in wrinkle depth. Their use for analysis of the photodamage phenomenon or the ageing process requires the addition of other parameters in the grading scale, specially skin colour. However

the addition of colour parameters in the scale makes them very difficult for visual assessment as it is affected by the individual's perception of colour.

Most grading systems suffer from low to moderate inter and intra observer agreements, as the assessment is based on visual perception of lines and wrinkles rather than actual physical measurements. Because of this and the subjective nature of these grading systems none have been adopted as a standard.

Developing an objective grading scale is not a trivial task since the quality of scoring is strongly influenced by the experience of the examiner, age, race [36], inter-observer agreement and intraobserver repeatability [37]. However it is possible to carry out an objective and quantitative analysis of wrinkles using 3D imaging devices but the slow acquisition speeds, dependence on replica production, and equipment cost makes them unsuitable for everyday clinical practice.

Researchers continue to use these grading systems and a downside of this is that the results from studies cannot be compared with 3D imaging analysis.

Studies on the pathogenesis of skin ageing as well as efficacy testing of cosmetic and aesthetic measures to prevent or reverse skin ageing require - as an easy to use method - a validated clinical score. A score that allows simultaneously assessment and differentiation between intrinsic and extrinsic skin ageing while taking into account the underlying skin type and potentially ethnicity. Such an

ideal score, however, doesn't exist currently.

2.5 Review of 3D Imaging Techniques

Numerous 2D and 3D imaging techniques exist for objective analysis of wrinkles and for efficacy evaluation of skin rejuvenation methods. Common to the majority of these techniques, is the use of replicas, with a few capable of carrying out an in-vivo analysis. However, the dependency on skin replica, slow acquisition speed and high cost makes them unsuitable for everyday clinical analysis. There are quite a few commercial devices available, these include the PRIMOS [38, 39] ,SkinChip [40], skin Visiometer [41], Visio face [42], Derma top [43], Skin Xpert, Image pro II, Reveal Imager, Omnia imaging system [44] and SIAscope [45].

The following sections discuss the principles of different 3D imaging techniques including the replica technique used for wrinkle analysis, its limitations, advantages and possible use in everyday clinical analysis.

2.5.1 Replica Technique

The inability to perform in-vivo measurements requires some of the skin profilometry techniques to use a skin replica, which necessitates the use of a reliable replicating material [46]. Based on the fluidity of material, hardening characteris-

tics, presence of artefacts and ease of use, Makki [47] came up with Silflo as the most suitable material to use.

Replica production is usually a two stage process; first a replica is made directly from the skin which provides a negative impression of microrelief. This is followed by producing a positive replica made from the negative. The initial process is very sensitive to body movements [48] and can produce undesired artefacts during reproduction of the detailed skin relief. Another problem associated with the method is the presence of air bubbles in the resulting compound due to improper mixing of materials. The extent of air bubbles in a replica depends strongly on the fluidity of the material used and its hardening characteristics [49]. The type of material used and the catalyst determine the hardening time of the replica and any shrinking during solidification, leading to further inaccuracies in the reproduction of relief [50]. Despite these inaccuracies in its construction and analysis, the replica technique is considered to be the gold standard [51]. The production of the replica often forms the first stage of a follow-on measurement procedure.

2.5.2 Mechanical Microscopy

This technique is based on a principle of scanning the surface relief line by line using a fine physical stylus or a probe. The vertical movement of stylus gives a

measure of the height of each point of the surface being examined.

There are quite a few drawbacks associated with this technique which makes it unsuitable for everyday clinical analysis. It has considerably low scanning speeds [46]. The measurements are strongly affected by the size of measuring stylus [52] and the replica used for measurements are often not hard enough so usually a hard counter replica has to be used. Nevertheless it can produce reliable measurements and the data is often used to measure accuracy of other optical systems.

2.5.3 Laser Triangulation

As the name suggests, laser triangulation is usually based on three components: a camera, the target surface and a laser emitter that form a triangle to determine the height variation of the surface. Jaspers et. al. [53] made use of this technique to study skin microrelief in vivo and a multitude of analysis was done related to skin ageing, irritation, hydration and skin extension. This measurement technique has a reasonable resolution and acquisition time but the measurement area is quite small [53].

2.5.4 Fringe Projection

Fringe projection uses a parallel strip pattern that is projected on the surface and is captured using a camera. The elevations and depressions in the surface cause the parallel stripes to deflect, which gives a measure of skin topography [54]. Compared to other 3D imaging techniques, fringe projection provides high acquisition speeds but at the expense of costly equipment and smaller measurement fields [38].

2.5.5 Light Transmission

The light transmission technique uses a blue dyed replica whose light absorption is known. The replica is lit from behind and it absorbs light depending on the thickness of replica. The transmitted light is captured with a camera and the intensity is calculated using Beer's Lambert's law, which is used for calculation of replica heights and depths [55]. It is very sensitive to the presence of artefacts in the replica production. Any bubbles in the replica can alter the intensity of the transmitted light and hence the recovered height. That is why it also requires the use of a special vacuum pump for mixing of two silicone components [41].

2.5.6 Photometric Stereo

Since the emergence of photometric stereo [56], the technique has developed into a recognised approach for 3D object shape recovery using a relatively simple methodology. The classical application of photometric stereo has been based on the interaction of collimated, uniform lighting with continuous smooth, Lambertian (diffusely reflective) surfaces. Photometric stereo uses a single sensor and multiplexed light to achieve multiple views of the same scene with differences only in the source lighting directions. This may be regarded as a form of temporal multiplexing, which is the key to the process. That is, light is provided at different times from differently positioned sources to allow the acquisition system to capture shaded images in isolation. From this we can resolve the surface gradient and reflectance of the surface under inspection.

In our context, the technique exhibits weaknesses and there are a number of challenges to overcome; firstly, skin has a complex reflection mechanism (i.e. not ideally Lambertian), secondly, in our case, the object cannot be considered static and thirdly conventional photometric stereo alone is not able to recover accurate geometry of the object in a metrology application. However, photometric stereo has been successfully used in acquiring skin texture for the purposes of pigmented lesion analysis [57–59] . The technique is based on the assumption

that skin does predominantly exhibits diffuse and specular reflection behaviour. This suggests a promise in applicability of the method for the acquisition of wrinkle topography. Multiplexing can be performed in a spatial and spectral fashion [60, 61] this may help to mitigate the effects of mixed mode reflection and improve the speed of acquisition in order to be able to image moving objects.

Different currently available photographic techniques record different aspects of skin appearance, each providing its own incomplete description. This limits their usefulness, especially for skin analysis. This study aims to develop a methodology using photometric stereo to recover detailed facial skin topography by addressing particular shortcomings and by developing new models. This will allow high resolution three dimensional topographical and reflectance maps to be produced in vivo without the need for a replica at a clinically acceptable speed $(< 0.5s)$.

Table 2.1: Comparison of photometric stereo with other imaging techniques.

	Cost	Computation/Acquisiton speed	Accuracy	Resolution	Calibration
LAT	Good	Average	Average	Average	Good
LT	poor	Average	Average	Good	Good
FP	Poor	Average	Good	Good	Average
GS	Good	Average	Average	Average	Good
MM	Average	Average	Good	Good	Average
PS	Good	Good	Average	Good	Good

Where

- LAT stands for Laser triangulation.
- LT stands for Light transmission.
- FP stands for Fringe projection.
- GS stands for Geometric stereo.
- MM stands for Mechanical microscopy.
- PS stands for Photometric stereo.

Table 2.1 shows a comparison of alternative imaging techniques with photometric stereo. Each system is ranked among 3 categories from poor, average and good. The criterion for comparison is based on the cost of equipment, its accuracy, computation time (including acquisition time), resolution and ease of calibration.

Since there are variety of systems available based on the same imaging technique; the exact cost, accuracy, resolution are not reported in the table as it can vary depending on the model. Overall the photometric stereo technique compares well with other methods specially in terms of acquisition speeds, cost and resolution however it has limited accuracy because of the Lambertian assumption associated with it.

2.6 Simulation Based Analysis of Skin Topography

Some simulation based analysis was done by Yamanda et al. [62] for cosmetic evaluation. It models the skin as a multilayer structure with most of the light reflected from the skin coming from inside of the skin. A subsequent analysis using the Monte-carlo method showed that total internal reflection plays an important role in suppressing a large portion of radiation going out through the skin surface. The experimental study also showed that skin texture and the presence of cosmetics have an effect on adjectives: directional and hemispherical reflectivity, the spectral quantity of these reflectivity measures and total internal reflection.

A weakness in this model is its assumption that the upper surface is smooth. So there is a need for improvement by addition of information regarding surface microstructure in this model and to see its effect on incoming light.

2.7 Parameters Commonly Used to Characterise Surfaces

Several different parameters have been used to characterise skin topography at different scales. At a micro level the skin has an anisotropic structure and as a result of ageing there is distortion and loss of secondary lines and changes in

orientation of primary and secondary lines. Based on a Fast Fourier Transform (FFT), Setaro [63] came up with a parameter called an irregularity skin index (ISI) and used it to quantify skin microrelief variations due to age. Some other parameters that have been used for analysis of anisotropy and roughness of skin include variation coefficient VC1 [64], Fourier analysis [65], autocorrelation [66] and patchwork method [67].

ISO/DIN defines many parameters for analysis of metal surface texture. These parameters are a collection of amplitude/height, spatial, functional and hybrid parameters. Most of the parameters used for quantification of skin have been taken from these ISO/DIN parameters. However skin relief is quite different from metal and does not show the same regularities as observed in metals. Skin topography is also anisotropic, hence there is need to define a standard parameter set that is adaptable to skin and which can uniquely characterise different skin topographies. Most 3D imaging techniques have used a variety of surface parameters like S_a, S_p, S_{max}, S_z [39, 43] while some have used their equivalent in profilometry like R_a, R_t, R_z, R_m [41, 42, 64] and very few used the waviness profile for analysis [65]. Standardisation of these parameters for their use with skin will also eventually help in comparison of results from different 3D imaging techniques.

It would be interesting to see how the surface and 3D aerial parameters defined in

the ISO 25178 [68] help in characterisation and quantification of skin topography. Especially the S- parameters set including texture direction and fractal dimension parameters as well as the volumetric parameters (or V- parameter set), where functional properties like fluid retention could be related to loss microrelief texture and deepening of primary lines. Also need to look at hybrid parameters e.g. height and spatial parameters.

Surface topography is three dimensional in nature and any measurement and analysis of 2D profiles gives an incomplete description of the real surface topography. The problem with an average roughness value R_a is that it does not make any distinction between peaks and valleys in a profile. Also it does not provide spatial structure information. Hence it is possible to have two different profiles with the same R_a value.

None of the existing 3D evaluation techniques have included an analysis of skin colour changes as a result of ageing or photodamage and there are no parameters defined for this. Also needed to allow comparative measurement is the standardisation of the measurement area and the set of roughness parameters and their intended scale.

2.8 Discussion

Current classification systems for wrinkles and micorelief in general are inadequate as a result of their qualitative nature and inherent problems with inter-user reproducibility.

3D in vivo profilometry provides objective analysis of skin microrelief and enables clinicians to predict and analyse the limitations and efficacy of various aesthetic procedures. Recently there has been a shift toward 3D non invasive and in vivo measurements of skin roughness, however whilst numerous 3D techniques have been developed and used, none of them has been adopted as a standard.

From the review of the current classifications as well as the current theories of skin classification, the ideal system has to be able to accurately measure the 3D topography of the skin microrelief. Moreover it should be able to do so in a way which produces objective, useful and reproducible surface quantification parameters, including average wrinkle depth and width as well as maximal wrinkle depth and width and wrinkle volume. It should also be able to take into account the optical properties of skin so as to be able to fully evaluate its baseline status and the result of any treatments upon it. Finally it needs to be both economical and fast enough for clinical usage.

The current reliance on replica techniques limits 3D systems to a purely external

superficial appreciation of the appearance of a surface. They are also time consuming and costly. The advent of new techniques such as 3D Photometric stereo may become the basis of a new series of microrelief measures. Also unlike many other 3D imaging techniques photometric stereo can recover concomitant colour information which is vital in the analysis of photodamage. To the best of author's knowledge, there has been little work done using photometric stereo in relation to the assessment of skin ageing, photodamage or scar analysis. Also the traditional photometric stereo technique is not accurate when it comes to imaging human skin. This thesis describes an improved photometric stereo technique that takes into consideration the complex optics of human skin in order to get more accurate 3D shape of skin.

Chapter 3

Photometric Stereo and Reflectance Models

Photometric stereo is a technique that estimates the surface normals of an object by observing it under different lighting directions. In its basic form it assumes that the surface under consideration obeys the Lambertian reflectance model. A surface is said to be Lambertian if the amount of light reflected by it is proportional to the cosine of the angle between the surface normal and light source direction. Such a surface appears to be equally bright irrespective of the observers viewing angle. Hence the reflected intensity of a point on a Lambertian surface is given by:

$$I = \rho E(N.L) = \rho E \cos\theta \tag{3.1}$$

- where E is the irradiance (incident power per unit area).
- N is the surface normal.
- L is the light source direction.
- ρ is the surface albedo.

If the surface is defined as a height function $z = S(x,y)$, its surface gradients in x and y directions are given by:

$$\mathbf{N} = \left[\frac{\partial z}{\partial x}, \frac{\partial z}{\partial y}, -1\right]^T = [p, q, -1]^T \tag{3.2}$$

Each point on a surface can be considered to be made of a facet (shown in Fig. 3.1) and the orientation of this facet is given by the normal vector N. The normal vector N is given by the cross product of two non-parallel tangents lying on the facet as:

$$g_x = [\partial_x, 0, p\partial_x]^T \equiv [1, 0, p] \tag{3.3}$$

$$g_y = [0, \partial_y, q\partial_y]^T \equiv [0, 1, q] \tag{3.4}$$

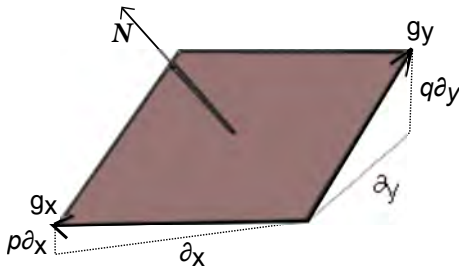

Figure 3.1: A graphical representation of facet.

By taking the cross product of these two vectors we can obtain the vector perpendicular to facet plane.[1]

$$g_x \times g_y = [\text{-}p, \text{-}q, 1] \tag{3.5}$$

Where p and q are used to determine the slope of this facet and after normalisation this becomes:

$$N = \frac{[-p, -q, 1]^T}{\sqrt{p^2 + q^2 + 1}} \tag{3.6}$$

For photometric stereo, Lamberts law may be written in matrix form as:

$$I = \rho \mathbf{L}.\mathbf{N} = \rho \begin{bmatrix} L_x \\ L_y \\ L_z \end{bmatrix}^T \begin{bmatrix} N_x \\ N_y \\ N_z \end{bmatrix} \tag{3.7}$$

[1] Mathematical Derivation of Eq. 3.5 is in Appendix B

Where $\mathbf{N}$ is the unit surface normal and L is the light source direction. A three source photometric stereo system can then be written in a matrix equation:

$$\begin{bmatrix} L_x^1 L_y^1 L_z^1 \\ L_x^2 L_y^2 L_z^2 \\ L_x^3 L_y^3 L_z^3 \end{bmatrix}^{-1} \begin{bmatrix} I_1 \\ I_2 \\ I_3 \end{bmatrix} = \rho \begin{bmatrix} N_x \\ N_y \\ N_z \end{bmatrix} = \begin{bmatrix} m_x \\ m_y \\ m_z \end{bmatrix} \tag{3.8}$$

Where $I = [I_1, I_2, I_3]$ is the intensity of a pixel resulting from varying illumination direction given by L. From eq. 3.8 the gradients in x and y directions can be calculated as:

$$p = -\frac{m_x}{m_z}, \quad q = -\frac{m_y}{m_z}, \quad \rho = \sqrt{m_x^2 + m_y^2 + m_z^2} \tag{3.9}$$

Where ρ is the albedo of the surface with normal N and L is the illumination vector.

3.1 Reflectance Models

As discussed previously most surfaces exhibit three main types of light interaction, these are absorption, transmission and reflection. Several models exist that describe this complex interaction of light with different materials. These models can be categorised into theoretical, empirical and simulation based models.

Some of these models can be used to describe the absorption and transmission characteristics of surfaces that are translucent while others are limited to opaque materials. The following sections will discuss different BRDF models and their particular features.

3.1.1 Lambertian Model

The Lambertian model is one of the simplest reflectance models and it describes the light interaction with a surface as ideal diffuse, meaning a surface appears equally bright from all viewing directions, hence making the model independent of the viewing direction. Most real world surfaces are not Lambertian, however due to its simplicity, this model is frequently used with photometric stereo to recover surface normals. According to this model the amount of reflected light from a surface is dependent on the angle between the surface normal $\vec{\mathbf{N}}$ and the light source direction $\vec{\mathbf{L}}$.

$$I(\omega_i) = \frac{k_d}{\pi} E \cos\theta_i = \frac{k_d}{\pi} E(n \cdot l) \tag{3.10}$$

Where E is the intensity of light source or irradiance and k_d is the diffuse re-

flection coefficient. ω_i is the incident radiance and θ_i is the zenith angle of incident light. Division by π in the denominator is included for energy conservation. Real world surfaces cannot be accurately modelled by just using a Lambertian model particularly if they are glossy or shiny because the specular component is not accounted for.

The geometry of incident illumination $\overrightarrow{L}$, viewing direction $\overrightarrow{V}$, surface normal $\overrightarrow{N}$, reflection $\overrightarrow{R}$ and Halfway vector $\overrightarrow{H}$ will be used from now on in most of the reflectance models and is shown in Fig. 3.2.

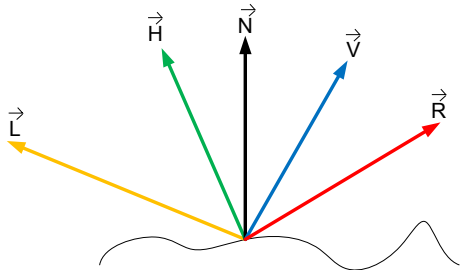

Figure 3.2: Arrangement of incident, viewing, halfway and reflection vector.

3.1.2 Phong and Blinn-Phong Model

The Phong reflectance model (eq. 3.11) is composed of both a diffuse and a specular component. The specular fall off is determined by the angle θ_s which is the angle between $\vec{\mathbf{R}}$ and $\vec{\mathbf{V}}$. The variable α determines the size of the lobe, where a higher α will result in sharp lobe while a lower value will produce a wide specular lobe.

$$I = (I_a + k_d(\cos\theta_i) + k_s(\cos\theta_s)^\alpha) \tag{3.11}$$

I_a is the ambient term while k_d and k_s are the diffuse and specular reflection coefficients.

To make it more computationally efficient Blinn replaced the reflection vector with the Halfway vector defined by:

$$\vec{\mathbf{H}} = \frac{\vec{\mathbf{L}} + \vec{\mathbf{V}}}{|\vec{\mathbf{L}} + \vec{\mathbf{V}}|} \tag{3.12}$$

So the Blinn-Phong model is written as:

$$I = (I_a + k_d(\cos\theta_i) + k_s(\cos\theta_h)^\alpha) \tag{3.13}$$

$$I = I_a + k_d(\vec{\mathbf{L}} \cdot \vec{\mathbf{N}}) + k_s(\vec{\mathbf{N}} \cdot \vec{\mathbf{H}})^\alpha \tag{3.14}$$

In summary, all the components involved in Blinn and Blinn-Phong model are:

- I_a is the ambient term.

- k_d and k_s are the diffuse and specular reflection coefficients.
- $\vec{\mathbf{L}}$ is the direction of light source.
- $\vec{\mathbf{V}}$ is the viewing vector.
- $\vec{\mathbf{H}}$ is the unit Halfway vector.
- $\vec{\mathbf{N}}$ is the surface normal.
- $\vec{\mathbf{R}}$ is the vector for reflected light,
- α is the specular fall off and its value determines the size of the lobe.

3.1.3 Oren Nayer Model

The Oren Nayer model provides a more realistic approach to rough surfaces by providing more reflected radiance for retroreflection (i.e. when the viewing direction approaches the direction of incidence). Most rough surfaces like clay, plastics exhibit increased reflected radiance at retroreflection angles which cannot be accurately modelled by a Lambertian model as the Lambertian model produces dark effects at occluding boundaries for rough surfaces. This model is based on the microfacet theory in which the surface is considered to be made of v-shaped cavities.

$$I(\omega_o, \omega_i) = \frac{\rho_d}{\pi} \left(A + B \cdot \max\left(0, \cos\phi_i - \phi_o\right) \cdot \sin\alpha \tan\beta\right), \tag{3.15}$$

Where

$$A = 1 - \frac{1}{2} \frac{\sigma^2}{(\sigma^2 + 0.33)} \tag{3.16}$$

$$B = 0.45 \frac{\sigma^2}{\sigma^2 + 0.09} \tag{3.17}$$

$$\alpha = \max(\theta_i, \theta_o), \quad \beta = \min(\theta_i, \theta_o). \tag{3.18}$$

The ω_o and ω_i terms represent the incident and reflected radiance.

3.1.4 Torrance-Sparrow Model

The Torrance and Sparrow model [69] is also a microfacet based model, however it differs from the Oren Nayer model by modelling each microfacet as a perfect reflector as apposed to a perfect diffuser. The modelling of a surface as a group of microfacets originates from the fields of optics and radiation transfer.

$$f_s = \rho_s * \frac{1}{\pi} * \frac{FDG}{(\vec{N} \cdot \vec{V})(\vec{N} \cdot L)} \tag{3.19}$$

where the term D determines the microfacet distribution . Each microfacet is con-

sidered to be perfectly specular. F is the Fresnel reflection, and the parameter G (Geometric attenuation factor) contributes the amount of light after masking and shadowing of the microfacets.

The Fresnel term describes the amount of light reflected due to the refraction index of the material at a particular incident angle. The Fresnel equation describes the ratio for reflected light as:

$$F = \frac{1}{2} * (\frac{\sin^2(\phi - \theta)}{\sin^2(\phi + \theta)} + \frac{\tan^2(\phi - \theta)}{\tan^2(\phi - \theta)}) \tag{3.20}$$

Where θ and ϕ are zenith and azimuth angles in spherical coordinates. Usually an approximation of Fresnel is used as the exact Fresnel equation is quite complex. An approximation of Fresnel equation was given by Schlick [70] which has proven to be accurate for most materials.

$$F(\theta_i) = F_o + (1 - F_o)(1 - \cos(\theta_i))^5$$

F_o is the measured Fresnel reflectance at normal incidence angle and θ_i is the angle of incidence. Another frequently used approximation to the Fresnel term

used is:

$$F = \frac{1}{2}\frac{(g-c)^2}{(g+c)^2}(1+\frac{[c(g+c)-1]^2}{[c(g-c)-1]^2}) \tag{3.21}$$

where $c = \cos(\phi) = \vec{L}\cdot\vec{H}$, η is the index of refraction and $g^2 = \eta^2 + c^2 - 1$.

Since it is a microfacet based model, it uses the Beckman distribution [71] to define the microfacet orientation distribution by applying the Halfway vector to determine the overall roughness of the surface.

$$D = \frac{1}{m^2\cos^4\alpha}e^{-(\tan\alpha/m)^2} \tag{3.22}$$

α is the angle between $\vec{N}$ and $\vec{H}$ and m is the root mean square slope of the microfacets. For small values of m the reflection becomes highly directional while for higher values of m the reflection is more spread out.

The geometric attenuation factor is given by:

$$G = \min\left\{1, \frac{2(\vec{N}\cdot\vec{H})(\vec{N}\cdot\vec{V})}{(\vec{V}\cdot\vec{H})}, \frac{2(\vec{N}\cdot\vec{H})(\vec{N}\cdot\vec{L})}{(\vec{V}\cdot\vec{H})}\right\} \tag{3.23}$$

$$G_1 = \frac{2(\vec{N}\cdot\vec{H})(\vec{N}\cdot\vec{V})}{(\vec{V}\cdot\vec{H})} \tag{3.24}$$

$$G_2 = \frac{2(\vec{N}\cdot\vec{H})(\vec{N}\cdot\vec{L})}{(\vec{V}\cdot\vec{H})} \tag{3.25}$$

Where 3.24 is the light blocked from the viewer and 3.25 is for the light considered to be in shadow. The geometric attenuation factor handles the shadowing and masking of the microfacets and calculates the resulting amount of light remaining after these effects. Its value ranges between 0 to 1 for completely shadowed(0) to no shadowing(1).

3.1.5 Ward Model

The Ward reflectance model [72] is an empirical model that has been used for modelling of both isotropic and anisotropic reflection. Due to anisotropic reflection, the surface exhibits varying reflectance when it is rotated about the surface normal. This phenomenon is common in materials like: clothing (e.g. velvet), brushed steel, hairs etc. The BRDF is:

$$I(\omega_o,\omega_i) = \frac{\rho_d}{\pi} + \rho_s \frac{1}{\sqrt{\cos\theta_i \cos\theta_o}} \frac{exp\left(-\tan^2\theta_h \cdot \left(\frac{\cos^2\phi_h}{\sigma_x^2} + \frac{\sin^2\phi_h}{\sigma_y^2}\right)\right)}{4\pi\sigma_T\sigma_B}. \tag{3.26}$$

σ_x and σ_y control the width of two lobes in two directions of anisotropy, while the lobe becomes isotropic when $\sigma_x = \sigma_y$

For isotropic reflection the Ward BRDF is written as:

$$f_r(x, \omega_o, \omega_i) = \frac{\rho_d}{\pi} + \rho_s \frac{1}{\sqrt{\cos\theta_i \cos\theta_o}} \frac{exp\left(-\frac{\tan^2\theta_h}{\sigma^2}\right)}{4\pi\sigma^2}. \tag{3.27}$$

3.2 Discussion

Several isotropic and anisotropic models also exist that try to model the complex interaction of light with materials. The choice of a reflectance function for a particular material however depends on the ability of a model to fit the actual reflectance of that material. Some of these models are good for real time shading due to their simplicity and computational cost, others are however intended for more realistic modeling for light interaction with different surfaces. The following is a summary of different properties of these reflectance models.

- Blinn-Phong
  - Computationally efficient.
  - Does not support anisotropy.
  - Suitable for rough surfaces, plastics.

- Oren Nayer
  - Physical model.
  - Does not support anisotropy.
  - Suitable for matte, dirty surfaces, concrete, valvet clothing etc.
- Ward
  - Empirical model.
  - Supports anisotropy.
  - Suitable for wood, machined metals, clothing.
- Cook Torrance
  - Physical, microfacet based model.
  - Does not support anisotropy.
  - Suitable for metals, plastics.

Chapter 4

Interreflection Modelling of Skin

The presence of interreflection at concave parts of a surface can lead to underestimation of depth while using photometric stereo. When light falls on a concave surfaces, the opposite facets force light to bounce multiple times before sending it back to the viewer. Since photometric stereo assumes that light incident on a surface is reflected from the same point it underestimates the depth of concave surface as shown in Fig. 4.1. The amount of underestimation is dependent on

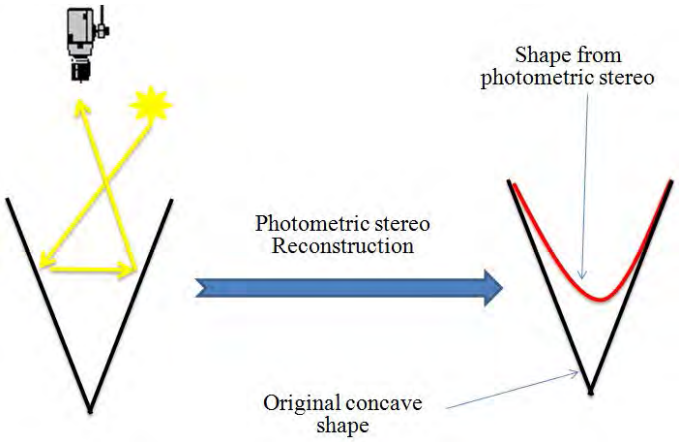

Figure 4.1: The underestimation of concave shape from photometric stereo.

the albedo of the surface i.e. a highly reflective surface will suffer from more interreflections than a lower reflective surface hence leading to more error in estimated shape.

This chapter introduces an implementation of a novel photometric stereo based technique for *in vivo* assessment of 3D skin topography in the presence of interreflections. To minimise the effects of interreflections, two methods are presented, one is based on the segmentation of areas containing interreflections and the other based on a spread of gradients due to variation in wavelength. The proposed methods illuminate skin with red, green, and blue coloured lights and use the resulting variation in surface gradients to mitigate the effects of interreflections. Experiments were carried out on Caucasian, Asian and African American subjects to demonstrate the accuracy of the method and to validate the measurements produced by the system. The methods produced significant improvement in 3D surface reconstruction for all Caucasian, Asian and African American skin types. The results also illustrate the differences in recovered skin topography due to non-diffuse BRDF for each colour illumination used, which also concur with the existing multispectral BRDF data available for skin.

4.1 Literature Survey

Since the emergence of photometric stereo [56], the technique has developed into a recognised approach for 3D object shape recovery using a relatively simple methodology. The classical application of photometric stereo has been based on the interaction of collimated, uniform lighting with continuous smooth, Lambertian (diffusely reflective) surfaces. Photometric stereo uses a single sensor and multiplexed light to achieve multiple images of the same scene with differences only in the source lighting directions. Most often this is achieved by a form of temporal multiplexing. That is, light is provided at different times from differently positioned sources, to allow the acquisition system to capture shaded images in isolated channels [73]. From this we can resolve the surface gradient and reflectance of the surface under inspection [57, 61] at a pixel or even sub-pixel resolution. However, accurate estimates of object geometry require that the surface reflectance properties and lighting conditions are known *a priori* and also most often assumes that the surface reflection is Lambertian.

The interreflection problem is a result of direct and indirect light reflection at the surface. Most concave surfaces exhibit such behaviour, as light bounces multiple times between patches on the surface before returning to the viewer. This phenomenon creates problems for shape for shading techniques, which for a given

albedo assume that the surface normal alone at a point defines the reflected radiance. On the other hand, the presence of interreflections can help resolve bas-relief ambiguity [74] and this is particularly useful in uncalibrated photometric stereo techniques where lighting properties are unknown [75].

Interreflections are also strongly dependent on surface albedo as investigated by Forsyth [76]. Objects with higher albedo values experience more interreflections than ones with lower albedo. Liao [4] used this distinction to separate direct and indirect reflected light by using coloured lights to vary surface albedo. However they did assume surface reflection to be Lambertian, which is also a prevailing assumption associated with skin when using shape from shading algorithms.

Nayar [3] proposed an iterative algorithm that refines an estimate of the actual shape and reflectance from an initial erroneous shape and reflectance approximation of a Lambertian surface. Most work related to interreflection has been aimed at opaque Lambertian objects, with the most relevant work done regarding interreflections in skin being based on the analysis of skin replicas [77, 78]. However the reflectance properties of replicas tend to be very different to that of skin. Replicas are often opaque while skin on the other hand is translucent and has complex reflectance properties which not only depend on the wavelength of light used but also on the type of skin (Asian, Caucasian etc.) under inspection

[79, 80].

Numerous studies involving the analysis of skin microrelief using photometric stereo have been conducted in the past decade, some are based on real time imaging whilst most are limited to static analysis. Tongbo et al. [81] proposed a method to extract skin microrelief using specular highlights, however the aquisition time to capture specular highlights for each point on the surface was considerably large as the method required illuminating the surface from a large number of distinct light directions. Micah et al. [82] used a contact based portable device to recover skin microrelief, however its accuracy was limited by the elastomer used as it could not reproduce fully large holes or groves. Several other non contact techniques exist, common to the majority of these techniques is that the analysis for accuracy of skin shape is qualitative and do not take into account the difference in reflectance from varying skin types (i.e. ethnicity) due to variation in illumination colour [83–85].

Infrared light has already been proven to offer advantage over white light [5] for skin imaging and was reported to exhibit a more diffuse reflection than visible light, suggesting a difference in BRDF between infrared and visible light. This chapter further investigates the effects of a change in illumination colour in the visible spectrum on the accuracy of 3D reconstruction of different skin types us-

ing photometric stereo. The following is a summary of key contributions presented in this chapter.

1. No published work has so far looked into the quantitative assessment of 3D skin microrelief using photometric stereo. Much of the analysis concerning the accuracy of skin microrelief is visually qualitative. The skin topography measurements presented in this chapter were validated using the PRIMOS 4 device and detailed experiments were performed with different skin types to determine the amount of error in surface normals and reconstructed height for each individual colour(R, G, B) and white light caused by differences in BRDF.

2. Earlier work regarding the surface accuracy analysis between infrared and white light showed that infrared was superior to white light in capturing accurate skin topography [5]. This chapter further contributes to the state-of-the-art by explaining the reasons for inaccurate acquisition of skin topography while using white light.

3. The development of a new technique for minimizing surface errors due to interreflection in the presence of wrinkles.

4. The development of a practical low-cost 3D capture system for static anal-

ysis of skin microrelief, which has its applications in efficacy evaluation of cosmetic treatments, surgical procedures and lesions analysis. The acquisition time of this system is shorter than most available commercial systems (as compared in section 2.5.6), has both a large field of view and depth of field, which allows observation of small scale variations (pores) to large wrinkles.

The following sections discuss issues concerning skin optics, skin reflectance and the BRDF of skin, as they are important factors in understanding the interreflection problem in skin and will form the basis of the proposed technique in order to diminish its effects.

4.2 Skin Optical Characteristics

Skin has a multi-layered structure, consisting of three main layers: epidermis, dermis and hypodermis (subcutis). These layers are different in structure and thickness from each other, and vary over different body regions [86]. They also vary among people of different origins [87]. The combined remittance of light from skin is composed of surface reflection, epidermal and dermal remittance. The surface reflectance is dependent on the change in refractive index from air to skin and is about 4-7% of the incident light, while the remainder comes from

lower layers. These lower layers define how much light is reflected back and how diffusely it is reflected.

Skin is not homogeneous and has complex optical properties. Aspects such as depth of penetration, scattering and absorption vary considerably as the wavelength varies from 400nm to 600nm [79]. Depth of penetration is the distance traveled by light before falling to (1/e) 37% of its initial value. For the range of wavelengths defined by the LEDs and filter used in the device, the depth of penetration for blue, green and red light is approximately 0.7mm, 0.9mm and 1.6mm respectively [79]. The variation is due to an increase in absorption at shorter wavelengths. Absorption in skin is mainly due to melanin and blood (oxy and deoxy-hemoglobin) in the epidermal and dermal layers and decreases as the wavelength increases in the visible spectrum [88, 89].

There are some differences concerning how diffusively skin reflects light based on wavelength. There is diffuse reflection due to interface roughness at the dermal-epidermal interface and shorter wavelengths (blue-green) are more sensitive to this than longer (red) wavelengths due to their lower penetration depth [90]. Longer wavelengths (towards red) are however more affected by multiple scatterings in the dermal layers; which consists predominantly of blood - due to absorption in the shorter wavelengths.

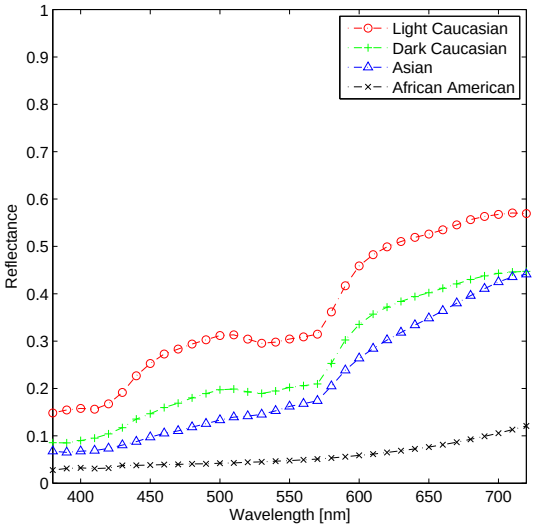

Figure 4.2: Multispectral reflectance of different skin types (NCSU skin reflectance data [1]).

4.3 Multispectral Reflectance of Skin

As a result of the complex optical properties, the resultant reflectance of skin appears as shown in Fig. 4.2. Over the entire visible spectrum, and for each skin type, the red part of the spectrum has the highest reflectance. This decreases as the wavelength of light decreases towards the blue part of the spectrum. This variation in reflectance as a function of wavelength is very important, as the interreflection phenomenon is closely related to the surface albedo/reflectance. The algorithm defined in section 4.7.3 utilizes this variation to acquire more accurate depth estimates for concave parts of the skin. Areas such as grooves/wrinkles in the skin are most susceptible to interreflections as the hollow rounded/v-shaped geometry force light to bounce multiple times before reaching the camera sensor. Given the variation of skin reflectance with wavelength, it can be deduced that

at concave parts of skin the chances of absorption of a photon increases after interreflection as the skin absorbs more light at shorter wavelengths, unlike at longer wavelengths where the possibility of photons reaching the camera sensor are greater as the skin absorption is lower.

4.4 BRDF of Skin as a Function of Wavelength

The BRDF describes how light is reflected from a surface. Its accurate description can improve the accuracy of shape from shading algorithms, such as photometric stereo, which assumes that the surface under inspection reflects light equally in all directions. BRDF is a function of incoming and outgoing light directions relative to the surface orientation. Also, it is a function of wavelength, as some materials absorb, reflect and transmit each wavelength differently. This is very much the case for skin. The BRDF function is written as:

$$BRDF(\theta_i, \phi_i, \theta_o, \phi_o, x, y, \lambda) \tag{4.1}$$

Where θ_x and ϕ_x represent incoming and outgoing direction in spherical coordinates, x and y represent spatial position and λ the wavelength. In its basic form, photometric stereo assumes that the surface under inspection has diffuse

reflectance at all wavelengths, which is not the case for skin. Most of the reported BRDF/BTF (Bidirectional Texture Function) measurements done for skin represent aggregates over the visible spectrum [91–93] and ignore variation in BRDF at specific wavelengths in the visible spectrum. The measurements done by [94, p. 2] were over 390nm to 710nm. These measurements were for a single reflected angle in order to see the variation in skin reflectance over the spectrum and did not take into account the variation for a wider range of reflection angles. Measurements undertaken by [95] were over 544nm and 633nm wavelengths using a CASI® scatterometer device.The device has an advantage of covering a range of incidence and reflected angles and provides a better understanding of the skin BRDF. These measurements show that there is considerable variation in BRDF of skin for these wavelengths. The impact of this variation on shape recovery at concave regions of skin is further discussed in section 4.7.2.

4.5 Materials and Methods

4.5.1 Photometric Stereo Setup and Acquisition

The photometric stereo skin imaging device presented here consists of four high power LEDs and an AVT Pike F100C camera[1] as shown in Fig. 4.3(a) . The cam-

[1] For details see datasheet in Appendix A

era has a resolution of 1000×1000 pixels and a colour depth of 8-bits. The acquisition time is approximately 0.6s and the measurement area is 65mm $\times 65$mm. The device has a 10.6mm depth of field and is able to recover both micro and macro 3D topography of skin as shown in Fig. 4.3(b). The LEDs used were 40

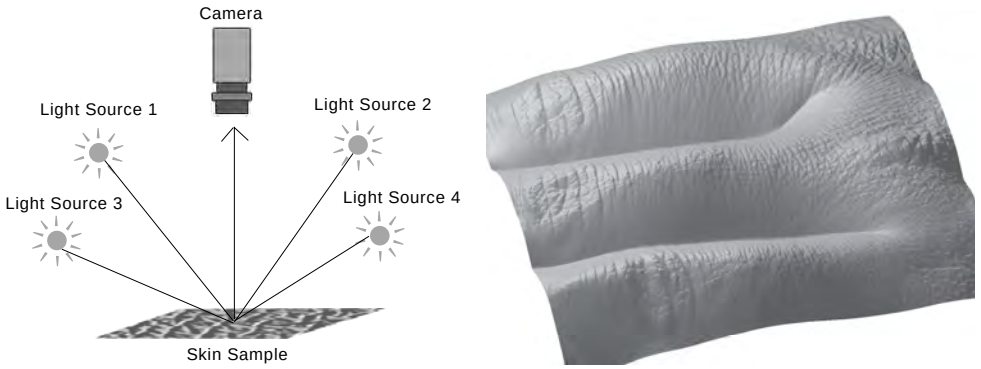

(a) (b)

Figure 4.3: (a) Schematics of the photometric stereo based 3D capture system. (b) The 3D skin macro and microrelief from the back of the hand acquired using the device.

Watt colour LEDs LZC-A0MD40[2] from LedEngin. These consist of a single emitter comprised of red, green, blue and white individually addressable dies. The dominant wavelength for each colour light is 625nm, 523nm and 462nm. The photometric stereo rig is designed to capture 12 images, four from each red, green and blue channel.

[2]For details see datasheet in Appendix A

4.5.2 Camera Calibration

The camera used in this experiment had a Kodak KAI-1020 sensor and its spectral response is shown in Fig. 4.4(a). The spectral response shows an overlap between each colour channel, there is variation in quantum efficiency for each channel and the sensor is sensitive between ultraviolet and infrared regions. In view of these constraints the imaging system was calibrated for colour correction and channel cross talk minimisation.

Colour correction is an important step in camera calibration as it enables generation of a device independent colour space from a device dependent colour space. This is usually performed by applying a 3-by-3 colour correction matrix (CCM) to the sensor R'G'B' data [96, 97]. For the camera used in this experiment, a device independent sRGB space was chosen and a CCM was formulated by minimising the RMS difference between the measured and original values of each colour block in the 24 patch MacBeth ColorChecker chart [98].

Due to pixel cross talk, more than one colour channel responds to a single colour light, as red light is picked up by the green and blue channels, green light produces a response in the red and blue channels, while blue light is seen by the red and green channels, causing an overall colour distortion. This channel cross talk

was minimised by using a Semrock FF01-457/530/628-23.3-D triband filter[3]. The filter also keeps the spectral response of the LEDs to a relatively narrow range of wavelengths as shown in Fig. 4.4(b) and cuts off the response of the camera below 450nm (close to ultraviolet) and above 650nm in the infrared region.

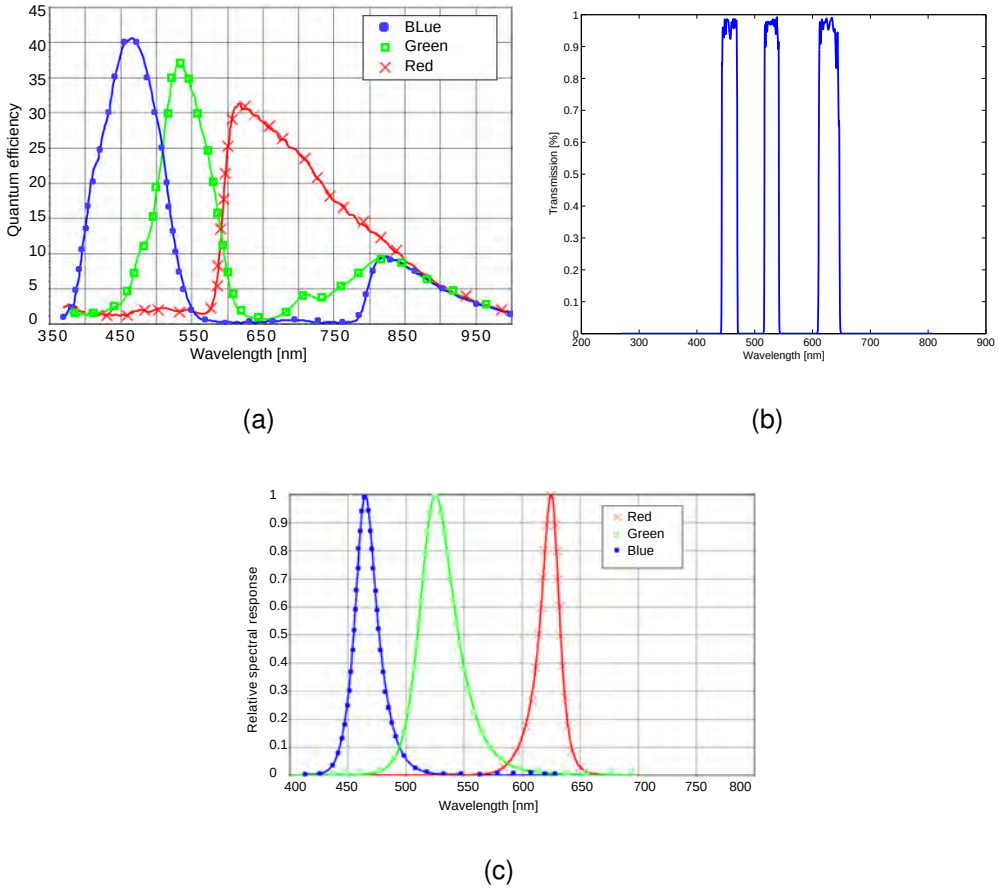

Figure 4.4: (a) CCD spectral response. (b) Triband filter response. (c) Spectral response of the LEDs

For the CCD response in Fig. 4.4(a), there is difference in quantum efficiency of all three channels and there are slight differences in transmission of each band-pass region of the triband filter. This means that equal exposures will not detect equal amounts in red, green and blue light. This can be overcome by either

[3]For details see datasheet in Appendix A

changing the camera gain or by varying the exposure time for each channel - a technique also used by [99, p. 83] to compensate for a reduced strength signal after scaling the exposure time. Both these methods have their own drawbacks- an increase in gain also increases the quantisation noise [100], while an increase in exposure time increases the signal dependent shot noise. The error in reconstructed height for skin resulting due to both quantisation and shot noise was compared. The error in reconstructed height was relatively less when the exposure time was varied and hence was selected for further analysis. Consequently, the exposure times for red and green light was kept longer than the blue and was controlled by varying the integrating time of the sensor. The sensor uses an electronic shutter and has light shielded areas to accumulate and transport the charges at the end of the integration period. A microcontroller was used to precisely control the integration times for each colour of light. Overall, this technique keeps the signal quantisation errors to a minimum and also avoids reduction in the signal to noise ratio.

Keeping in view the wavelength range limited by the triband filter, the patches in the last row of the MacBeth ColorChecker chart can be considered nearly spectrally neutral, meaning they reflect all colour bands equally. These patches were used to see whether the CCD recorded equal intensities of each red, green and

blue light after calibration for differences in quantum efficiency.

Section 4.6 and 4.7 explain the segmentation based and gradient spread based methods for minimisation of errors in shape due to interreflections.

4.6 Segmentation Based Method

4.6.1 Skin Replica and Ground Truth

To validate the measurements produced by the system four subjects were selected; among them, two were Caucasians and two Asians. The measurements were done on the forehead of all subjects by first imaging them directly using the photometric stereo device and then by producing a corresponding replica for the same skin location for each subject. All replicas were made using the SILFLO impression material. The material has excellent flow and hardening characteristics, can reproduce very fine skin texture and has been widely used for very fine replication of skin features [101–103]. These replicas were then imaged using a PRIMOS 4 device and used as a ground truth. The PRIMOS device operates on the principle of structured light 3D imaging and has already proven to work for wrinkles and scar evaluation and efficacy testing of skin treatments [38, 54, 104]. Its acquisition time is $<$100ms with a lateral and vertical resolution of 28μm and

2μm respectively. The PRIMOS device has also proven to give comparable results to a mechanical profilometer [53], and unlike photometric stereo its accuracy is not dependent on the reflectance properties of replica or skin as it uses the variation in projected pattern to recover height information. Hence the measurements from this device were used to verify the *in vivo* measurements produced by the photometric stereo device.

4.6.2 Error Analysis

A cross-sectional view of the wrinkled region obtained from the photometric stereo based device is shown in Fig. 4.5. It is clear that at concave parts of the skin (wrinkles) the error is significant for each colour light. The red light suffered the most from interreflections due to lower albedo and underestimated the wrinkle depth, while green and blue light overestimated the wrinkle depth due to non-diffuse BRDF. Since white light is an aggregate of all three colours it also overestimated the wrinkle, as it has one part of red and two parts of green and blue combined. However these errors in depth estimates were not only because of the integration of surface normals, there was exaggeration in the recovered slope from green and blue light while the red light underestimated the actual slope. Table 4.1 shows the

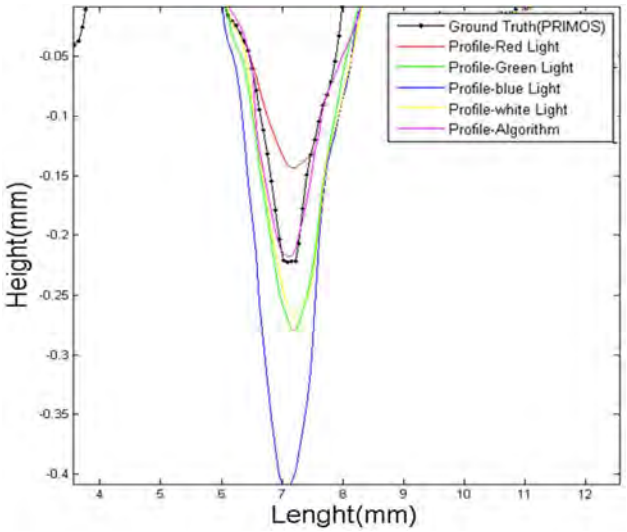

Figure 4.5: Cross-sectional view of the wrinkled region obtained from each colour light and the proposed algorithm.

root mean square (RMS) error in height for all subjects and for each individual colour light. The RMS error in height shows that the error is minimum while using red light for all subjects and it increases as the wavelength decreases from green towards blue light. Table 4.1 and 4.2 also show the improvement in depth estimates and surface normal after application of the algorithm which is explained in section 4.6.3.

Table 4.1: RMS error in height for each subject and the corresponding light used (subject 2, 3 were Asians and 1,4 Caucasians).

	RMS error				
	Red light	Green light	Blue light	White light	Proposed method
Subject 1	3.0967	3.6121	5.1534	3.5361	2.0581
Subject 2	1.1629	1.0340	2.1006	1.2643	0.8265
Subject 3	0.8796	1.0987	2.501	1.1161	0.3218
Subject 4	1.2343	2.3735	3.9193	1.9255	0.9172

4.6.3 Algorithm for Improved Depth Estimate

Since topographic skin recovery error is largely due to interreflection in the wrinkled part of the skin, segmentation of the region of interest (ROI) is necessary before application of the new algorithm. This is done by using the watershed algorithm [105]. The accuracy of the watershed algorithm in segmenting the ROI was found to be much better when the height map of the surface was used instead of a more conventional 2D image, which has the tendency to suffer from over segmentation [106]. The surface height map was calculated using a photometric stereo algorithm and was filtered using a 3D Gaussian filter to separate high frequency data from the underlying form. The 3D Gaussian filter function used was simply a product of two Gaussian filters [107] as shown in Eq. 4.2.

$$T(x,y) = \frac{1}{(\alpha_s^2.\lambda_{xc}.\lambda_{yc})} * exp[-[\pi(\frac{x}{(\alpha_s.\lambda_{xc})})^2 + \pi(\frac{y}{(\alpha_s.\lambda_{yc})})]^2] \tag{4.2}$$

Table 4.2: l2-Norm error for all subjects from each light and proposed method (subject 2, 3 were Asians and 1,4 Caucasians).

	RMS error				
	Red light	Green light	Blue light	White light	Proposed method
Subject 1	0.2442	0.3660	0.404	0.3471	0.2168
Subject 2	0.1823	0.2264	0.2929	0.2294	0.1766
Subject 3	0.2291	0.2986	0.3322	0.3164	0.1668
Subject 4	0.2802	0.3352	0.3844	0.3320	0.2711

Where $\alpha_s = 0.4697$ is a constant and λ_{xc}, λ_{yc} are cutoffs in x and y. The high frequency data was then fed into the watershed algorithm to segment the wrinkle. Fig. 4.6 shows the result of a segmented wrinkle for one of the subjects.

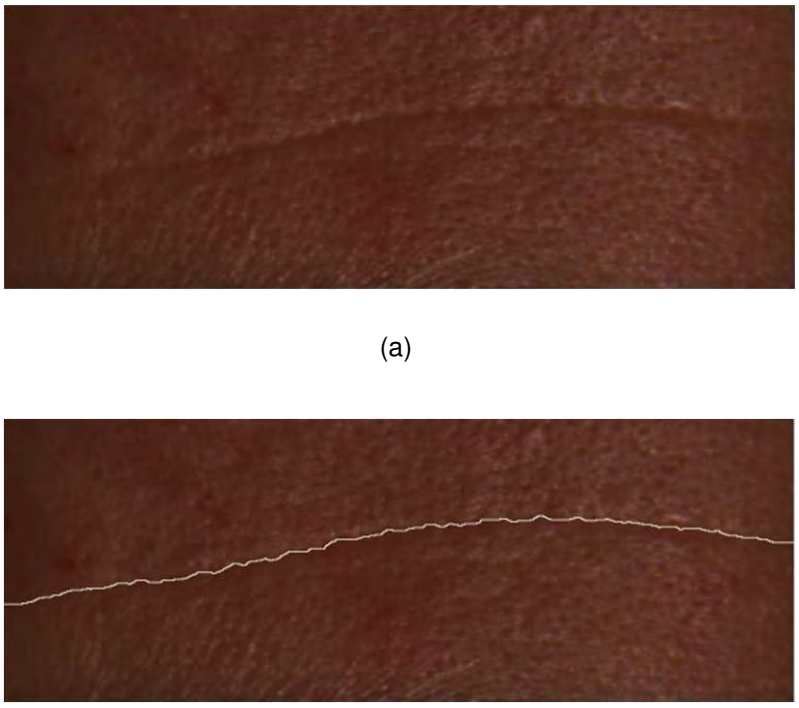

(a)

(b)

Figure 4.6: (a) original image. (b) Segmented wrinkle line using watershed algorithm.

The algorithm works by scaling gradients at wrinkled regions. The segmented line from the watershed algorithm provides the points where the gradients need to be scaled. The gradients from red light were used for the whole surface and then the algorithm modifies the gradient map by adding scaled gradients at the wrinkled region only. This modified gradient map is used to calculate an interim height map using the Frankot Chellappa's technique [108]. This interim height

map has values close to ground truth at the wrinkled region only. These values are substituted in the height map obtained from red light; this way the overall surface stays undisturbed except at the wrinkled region where there was underestimation of depth due to interreflection. The following pseudo code explains the steps involved in improvement of depth estimates.

Algorithm: Proposed algorithm to improve depth estimate

Input: 12 images (4 from each colour light)
Output: height Z_r .
1. Get location of segmented points (i_x, i_y).
2. Calculate gradients from each colour light $p_{red}, q_{red}, p_{green}, q_{green}, p_{blue}, q_{blue}$.

for all pixels
a) $T1 = (p_{red} + (p_{green} + p_{blue})/2)/2$
b) $T2 = (q_{red} + (q_{green} + q_{blue})/2)/2$
end for
1. Put $G1 = p_{red}$ and $G2 = q_{red}$

for all i_x, i_y
2. $G1(i_x, i_y) = T1(i_x, i_y)$
3. $G2(i_x, i_y) = T2(i_x, i_y)$
end for
4. Calculate height z_a from gradients G1,G2
5. Calculate height z_{red} from gradients p_{red}, q_{red}
6. Put $Z_r = z_{red}$

for all i_x, i_y
a) $Zr(i_x, i_y) = min\{z_a(i_x, i_y), z_{red}(i_x, i_y)\}$
end for

The algorithm minimised the errors when compared to white light and each R, G, B lights as shown in Table 4.1 and 4.2. Also the recovered shape of wrinkle from the algorithm counteracts the effects of any over and underestimation of wrinkle depth as shown in Fig. 4.7. The dotted line shows the ground truth from replica and the solid line profile is from the proposed algorithm. Overall the error was minimum for the algorithm when compared to all colour lights and subjects;

however the accuracy of algorithm is currently dependent on the segmentation process.

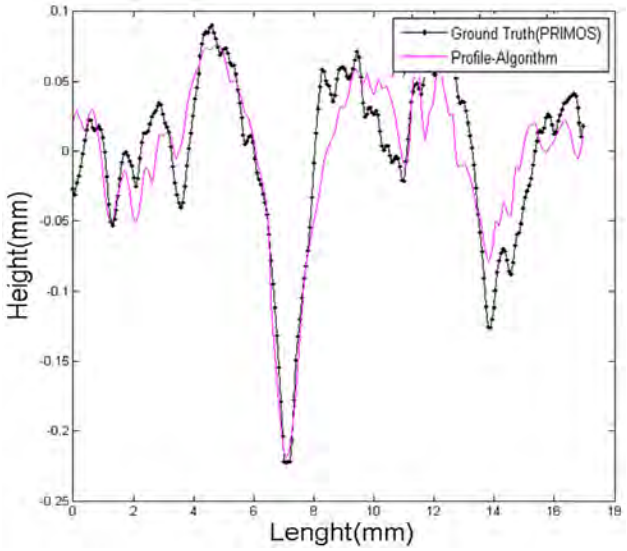

Figure 4.7: Comparison of algorithm with ground truth.

4.6.4 Skin Roughness Analysis

The skin microrelief is anisotropic and changes with increasing age [103]. Most of the 3D imaging techniques to date have used the parameters defined by the metal industry for quantification of skin microrelief. The parameters used are defined in the ISO 468, ISO 4287 and DIN 4762-4768 for the characterisation of metal surface [64]. The anisotropy and irregularity of skin relief makes characterisation of skin different from metal and that is why not all parameters are used for quantification of skin microrelief. The most commonly used parameters for roughness evaluation are R_a, R_z, R_p, R_t [46]. These parameters have been used

for analysis of age, effects of moisturizers, botox, sun damage, and have proved to be useful in characterisation of before and after effects of treatments. Three samples of forehead wrinkles representing low, moderate and high wrinkle states were used. Standard metal roughness parameters $R_a, R_q, R_{ku}, R_{sk}, R_p, R_v$ (Arithmetic mean, root mean square, kurtosis, skewness, largest profile peak height, largest profile valley depth respectively) along with Fractal box counting [109] and power spectrum based techniques were used to quantify skin topography. Standard algorithm [110] was implemented for calculation of R_a, R_q, R_{ku}, R_{sk}: For

Table 4.3: Roughness parameters and their definition.

Parameter	Definition
R_a	Arithmetic mean of the absolute values of Z(x) (profile height) within a sampling length.
R_q	Root mean square value of Z(x) within a sampling length.
R_{ku}	Kurtosis (degree of peakedness) of the assessed profile.
R_{sk}	Skewness of the assessed profile.
R_p	Largest profile peak height Z(x) within a sampling length.
R_v	Largest profile valley depth Z(x) within a sampling length.

each sample length $i = 1....CN$ (CN is the Calculation Number and its default value defined by ISO 4288 is five)

- Calculate

$$Ra_i = 1/l \int_0^l |Z(x)|dx$$

$$Rq_i = \sqrt{1/l \int_0^l Z^2(x)dx}$$

$$Rku_i = 1/(Rq_i)^4[1/l \int_0^l Z^4(x)dx]$$

$$Rsk_i = 1/(Rq_i)^3[1/l \int_0^l Z^3(x)dx]$$

- Calculate

$$Ra = 1/CN \sum_{i=1}^{CN} Ra_i$$

$$Rq = 1/CN \sum_{i=1}^{CN} Rq_i$$

$$Rku = 1/CN \sum_{i=1}^{CN} Rku_i$$

$$Rsk = 1/CN \sum_{i=1}^{CN} Rsk_i$$

The following algorithm was used for measurement for R_p and R_v. For each sample length $i = 1.....CN$

- Determine profile peaks (portions of the profile above the mean line Zp)
- Determine profile Valleys (portions of the profile below the mean line Zv)
- For each profile peak $j = 1...m$

  Calculate

  $$Rp_i = \max_{1 \le j \le m} Zpj$$

  $$Rv_i = \max_{1 \le j \le m} Zvj$$

  Calculate

  $$Rp = 1/CN \sum_{i=1}^{CN} Rp_i$$

$$Rv = 1/CN \sum_{i=1}^{CN} Rv_i$$

Table 4.4: Standard roughness and fractal dimension based Quantification for different wrinkle states.

Parameter	sample 1 (Low)	sample 2 (Moderate)	sample 3 (high)
R_a	10.4706μm	47.1366μm	54.2052μm
R_q	12.3165μm	57.3867μm	65.6712μm
R_{ku}	65.6712μm	144.1566μm	154.1547μm
R_{sk}	-4.1769μm	17.3754μm	-7.9632μm
R_p	22.3146μm	120.6135μm	132.804μm
R_v	132.804μm	100.4913μm	123.0453μm
Df(Box counting)	2.0792	2.0911	2.1167
Df(Power spectrum)	2.0573	2.0463	2.0995

Table 4.4 shows the quantitative comparison of three skin samples using conventional and fractal based techniques [111]. Unlike the conventional parameters for roughness analysis the fractal based technique does not require any high/ low pass filtering, and is independent of the anisotropy of skin (the orientation of surface does not affect the quantification) and makes use of complete 3D skin topography. Fractal dimension (Df) is a non-integer dimension between the Euclidean dimension and it depends on the complexity of the surface. Fractal dimension for profiles exit between $1 < Df < 2$ and for surfaces it lies between $2 < Df < 3$, it is equal to Euclidean dimension of 1 for a straight line, 2 for a flat plane and 3 for a cube. The power spectrum based fractal calculation was done using the Gwyddion software [111]. In the cube counting method for calculating fractal di-

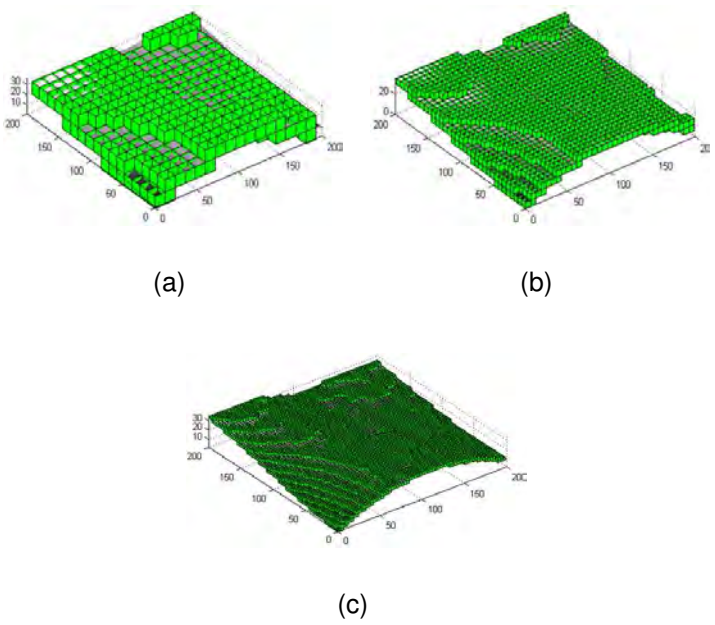

(a) (b)

(c)

Figure 4.8: (Graphical representation of cube size variation ((a) - (c)) used for the calculation of Fractal dimension for a patch of skin.

mension, cubes of size (s) are counted which cover the whole surface. The cube size is then varied and the number of interesting cubes N is counted. The log of cube count $Log(N(s))$ is then plotted against $Log(1/s)$ and the slope of the resulting plot gives the required fractal dimension. Fig 4.8 shows the variation of cube size in the cube mesh as it covers the whole surface. A comparison of skin roughness analysis using the conventional parameters and Fractal based technique shows that the resulting fractal dimension can be used in conjunction with 2D roughness parameters for quantitative evaluation different wrinkle severities.

4.7 Gradient Spread Method

4.7.1 Skin Replica and Ground Truth

Twenty two subjects were selected for this experiment; among them, ten were Caucasians, eight Asians and four African American. Only subjects with no history of skin condition/allergy with visible wrinkles on their forehead were selected. The measurements were done for all subjects in a cool dry place with constant temperature. The subjects were strictly advised not to use any makeup or moisturisers on their face and to make sure the skin surface was free of dust particles and sweat, the skin was gently wiped with a dry swab as dust particles or sweat can cause imperfection in the replica and in the recovered shape. The subjects were also asked to keep their eyes closed as it can alter the depth of wrinkles. The procedure involved imaging the skin directly using the photometric stereo device and then by producing a corresponding replica for the same skin location for each subject as shown in Fig. 4.9. All replicas were created using the same technique as described in section 4.6.1 and then imaged using a PRIMOS 4® device and used as a ground truth. The PRIMOS device has different spatial resolution and has a small measurement area compared to the photometric stereo device. First overlapping regions from both devices were extracted by using markers that

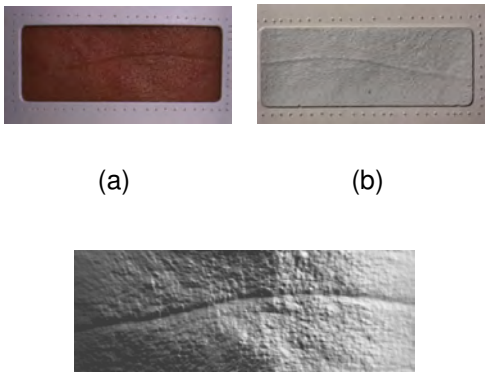

(a) (b)

(c)

Figure 4.9: (a) Forehead wrinkle directly imaged using photometric stereo device. (b) Corresponding replica. (c) *3D* reconstruction of skin images taken *in vivo*.

were added at the boundary of the replica as shown in Fig. 4.9(a) and 4.9(b). The data from Photometric stereo was then interpolated by using PRIMOS data as reference and finally the registration of both 3D data sets was achieved using the iterative closest point algorithm [112].

4.7.2 Error Analysis

Table 4.5 shows the root mean square (RMS) error in reconstructed surface height for all subjects and for each individual coloured light. The RMS error in height shows that the error is minimum while using red light for all subjects and it increases as the wavelength decreases from green towards blue light. Fig. 4.10(a) shows a 2D slice from the reconstructed height at the wrinkled part of the skin. It is clear that at concave parts of the skin (wrinkles) the error was significant

for each colour of light. Red light suffered the most from interreflections due to higher albedo and it underestimated the wrinkle depth, while green and blue light overestimated the wrinkle depth due to relatively non-diffuse BRDF [95].

Table 4.5: Mean and standard deviation (SD) of RMS error in height for each skin type and the corresponding light used.

		RMS error				
		Red light	Green light	Blue light	White light	Proposed method
Caucasian	Mean	1.3150	1.5212	2.2487	1.5105	0.7174
	SD	0.8565	0.9852	1.3722	0.9573	0.5180
Asian	Mean	1.3507	1.5409	3.02613	1.7294	0.7277
	SD	0.7797	0.9549	1.7022	1.0587	0.4911
African American	Mean	3.7145	5.7687	7.2140	5.7087	3.3183
	SD	1.5353	1.1518	1.5821	1.2263	0.7594

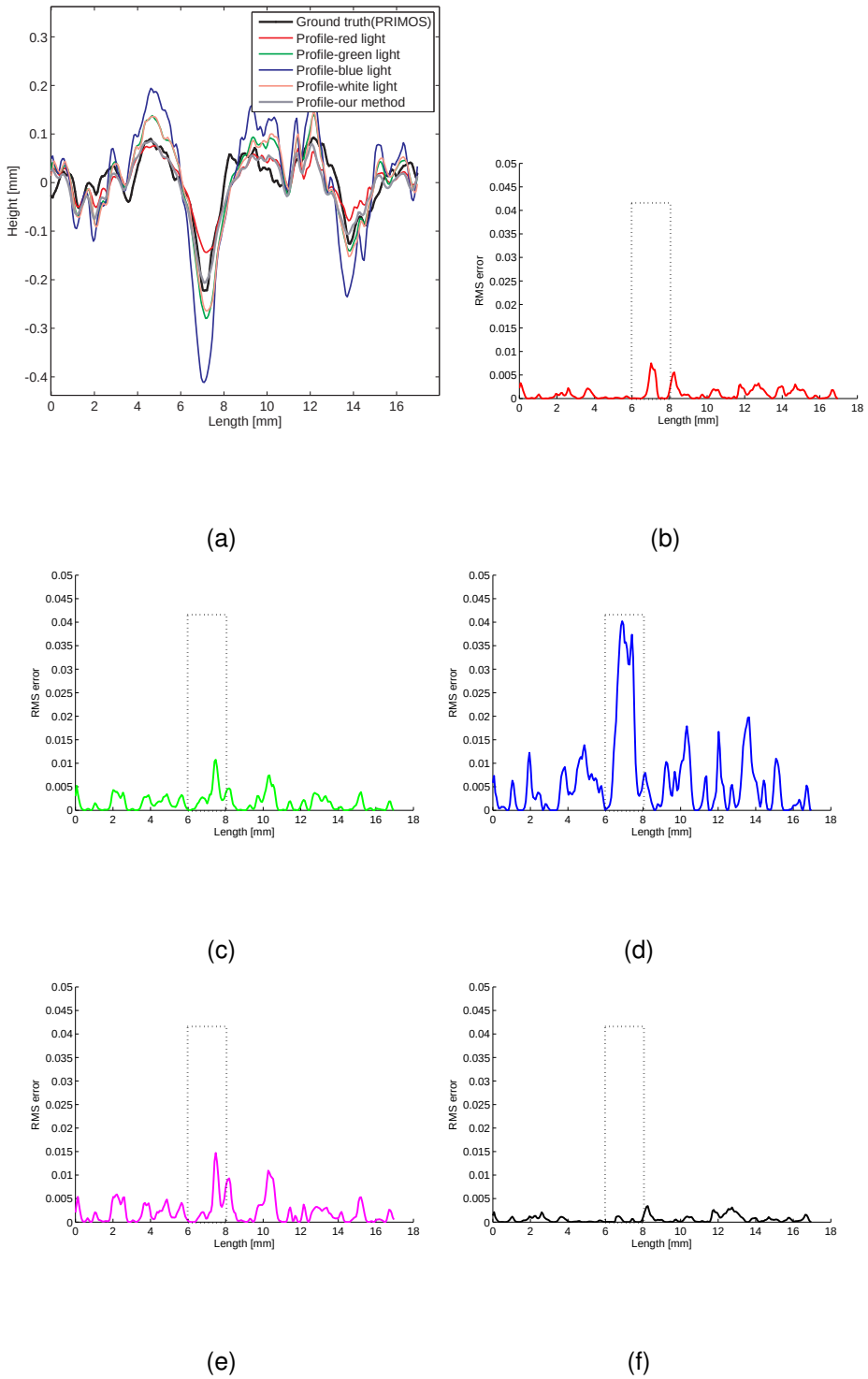

Figure 4.10: (a) 2D Profiles obtained for the wrinkled region from each colour light and the proposed method (The wrinkle lies between *6-8mm* length). (b)-(f) RMS error in height from red, green, blue, white light and the algorithm respectively (The dotted rectangular region points out the location of wrinkle).

Since white light is an aggregate of all three colours it also overestimated the wrinkle depth as it has one part of red and two parts of green and blue combined. Integration of surface normal data can introduce errors in the reconstruction of the surface. An analysis of surface slant angles without integration was carried out. At the wrinkled region and with reference to the slope estimation shown in Fig. 4.11, it is evident that the over and under estimation of surface normals from the three primary colour lights still occurs and that the error in reconstructed height is not just due to the integration method used. To minimise the error, the proposed method makes use of spectral variation of surface normals in gradient space, consequently making it free of the integration method used.

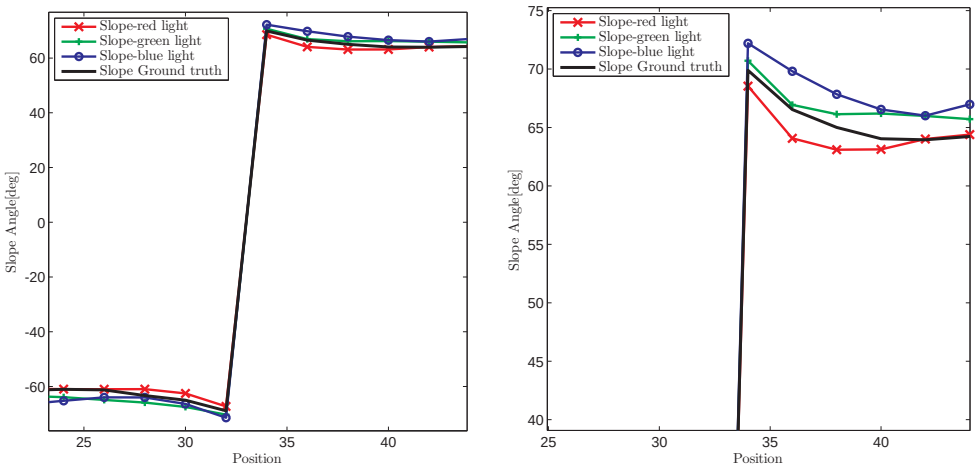

Figure 4.11: (a) Over and underestimation of slope from each (R, G, B) light at the wrinkled region (valley). The mid region data value rise represents lowest point of valley of wrinkle where slope changes sign. (b) Increased scale to show differences in slope from one side of valley.

4.7.3 Surface Normal Mapping in Gradient Space

Mapping of surface normal data in gradient space gives useful cues for finding a surface that has the right balance of fine scale and global topography. The gra-

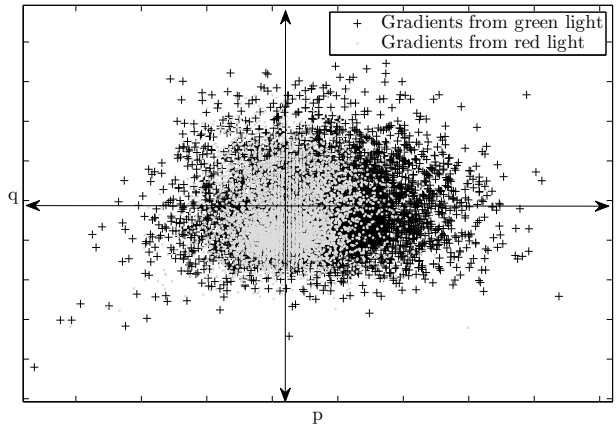

Figure 4.12: Gradient map obtained from red and green light (The center cluster of a lighter shading represents the group of gradients from red light).

dients from red and green colour light ($R(p,q), G(p,q)$) from Fig. 4.12 show that the gradients for a patch of surface are more spread from green light and they get more and more compactly contained for longer wavelengths towards the red light. This is mainly due to a smoothing effect under red light and the opposite effect under green light. By controlling the amount of spread in gradients from red light we can resolve a surface which has the right balance of high and low frequency data. This has been achieved by altering the orientation of the gradients from the directions obtained under red light towards the directions obtained under green light.

By fitting linear and quadratic functions between gradients recovered from each

R, G, B light ($R(p,q)$, $G(p,q)$ and $B(p,q)$), a bounding region is obtained as shown in Fig. 4.13. This bounded region provides the search space for finding the optimal gradient for each point. By defining a constraint in the Fourier domain the optimal point lying in the bounded region is obtained. This results in emulation of a surface that is closer to the ground truth.

The selection of an optimum point for each normal is difficult as the movement

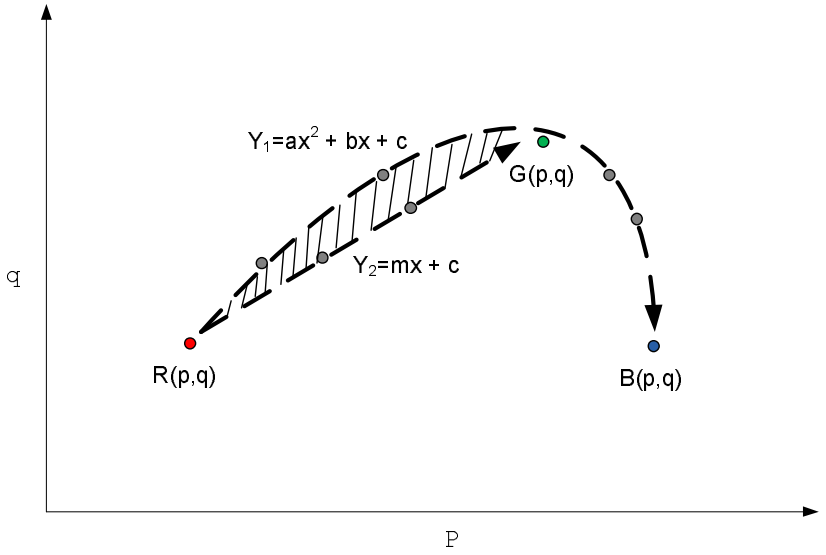

Figure 4.13: Movement of gradients from red light towards the green. The gradient set is calculated in the region bounded between quadratic and linear fits.

of gradients from red towards green is different for each point in the gradient map and for each skin type. Dong and Liang [113, 114] used Fourier analysis to obtain a perfect synthetic gradient map of a Lambertian surface and determined a constraint to extract diffuse components for different reflectance models. This constraint was used to find the optimum point in the gradient map that is closer to the ground truth for each skin type.

Given a surface described as a height function:

$$Z = S(x,y) \tag{4.3}$$

At a given point on a surface $S(x,y)$ the gradients in x and y directions are given as:

$$\text{grad}(S(x,y)) = (p(x,y), q(x,y)) = [\frac{\partial z(x,y)}{\partial x}, \frac{\partial z(x,y)}{\partial y}] \tag{4.4}$$

By taking the Fourier transform ($\mathscr{F}$) of each pair of surface gradients $p(x,y)$ and $q(x,y)$ we get their corresponding expressions in frequency domain *P(c, r), Q(c, r)* [4].

$$\mathscr{F}(p(x,y)) = P(c,r) = icH(c,r) \tag{4.5}$$

$$\mathscr{F}(q(x,y)) = Q(c,r) = irH(c,r) \tag{4.6}$$

[4] For details see mathematical derivation in Appendix B

Where $H(c,r)$ is the Fourier transform of the surface height map $S(x,y)$ and (c,r) represents the 2D spatial frequency coordinate. From Eq. 4.5 and 4.6

$$rP(c,r) = cQ(c,r) \tag{4.7}$$

Given the location of two points $p_r(x,y)$, $q_r(x,y)$ and $p_g(x,y)$, $q_g(x,y)$ in gradient space from red and green light respectively (Subscripts r and g are for red and green light), the gradients from red light are moved towards the green and a new location is acquired at $p_p(x,y)$, $q_q(x,y)$. By using a quadratic and linear fit function a new set of gradients is obtained for each point in the gradient map.

$$P_{1\ldots s}(x_1,y_1)\ldots P_{1\ldots s}(x_m,y_n) \text{ and } Q_{1\ldots s}(x_1,y_1)\ldots Q_{1\ldots s}(x_m,y_n) \tag{4.8}$$

Where $m \times n$ is the total number of points in the gradient map, s represents the number of points in the search space generated for a single location in gradient map. By minimising the constraint condition below proposed by Dong, the optimum gradient map was found from the set of gradients in 4.8.

$$|rP(c,r) - cQ(c,r)| \tag{4.9}$$

An inverse Fourier transform is taken of the optimum gradient map from Eq. 4.9 and integrated to get the resultant height map. Fig. 4.10(a) shows a profile of the resultant height obtained. The method emulates a surface that lies between the surfaces obtained from red and green light and is thus closer to the ground truth. It also minimises the underestimation of wrinkle depth and improves the overall accuracy in recovery of surface data for all Caucasian, Asian and African American skin types, as shown in Table 4.6 and 4.7.

4.7.4 Validation

The proposed technique uses gradients from red light as a base as it already has the minimum error in reconstructed height. It produces maximum variation at the wrinkled regions of the skin to compensate for underestimation of depth, however at relatively flatter parts of the skin it keeps the variation to a minimum, consequently keeping the estimated height close to the ground truth as shown in Fig. 4.10. The method was tested on all subjects and the RMS error in height and *l*2-norm error was calculated by comparison with PRIMOS ground truth data. The method produced significantly reduced error when compared to conventional white light or each R, G, B light as shown in Table. 4.6 and 4.7. Also, the wrinkled areas recovered using proposed technique minimises the effects of any over and

underestimation of wrinkle depth.

4.8 Discussion

The results in section 4.7.4 demonstrate the effectiveness of the proposed method and also shows that for overall skin geometry red light is less prone to error in comparison to using green, blue and white light as its accuracy suffered only at concave parts of the surface. However, the RMS and *l*2-norm error clearly indicate that the proposed technique further reduced the error when compared to each red, green, blue and white light.

The availability of multispectral skin BRDF data is scarce, as most measurements are taken using white light for a limited set of incoming and outgoing angles. There are currently no datasets that show dense BRDF measurements for different types of skin, over a range of wavelengths. Knowledge of skin BRDF is not

Table 4.6: Mean and standard deviation (SD) of RMS error in height for each skin type and the corresponding light used.

		RMS error				
		Red light	Green light	Blue light	White light	Proposed method
Caucasian	Mean	1.3150	1.5212	2.2487	1.5105	0.7174
	SD	0.8565	0.9852	1.3722	0.9573	0.5180
Asian	Mean	1.3507	1.5409	3.02613	1.7294	0.7277
	SD	0.7797	0.9549	1.7022	1.0587	0.4911
African American	Mean	3.7145	5.7687	7.2140	5.7087	3.3183
	SD	1.5353	1.1518	1.5821	1.2263	0.7594

Table 4.7: Mean and standard deviation (SD) of *l*2-norm error for all skin types and the corresponding light used.

		*l*2-norm error				
		Red light	Green light	Blue light	White light	Proposed method
Caucasian	Mean	0.1741	0.2162	0.3197	0.2073	0.1106
	SD	0.1263	0.0935	0.1997	0.0806	0.0611
Asian	Mean	0.2112	0.3357	0.3936	0.3527	0.1627
	SD	0.1333	0.1920	0.2207	0.2045	0.0885
African American	Mean	0.4881	0.6914	0.8066	0.6897	0.4161
	SD	0.1274	0.1490	0.1739	0.1439	0.1353

only important for realistic skin renderings but also for accurate 3D reconstruction of skin, as shape from shading algorithms are dependent on how light is reflected from the surface and how light distribution varies as a function of wavelength.

The interreflection problem is very significant for shape from shading techniques and it is not just the wrinkles in skin that suffer from interreflections; it would be interesting to see its effects on moles, lesions, keloid, burn and surgical scars, as these can appear as an elevated skin growth or an indentation in the skin, and usually have a different colour when compared to the surrounding skin. This difference in colour would define the amount of interreflections at the boundary of the elevated skin growth. However, for indented skin, the degree of concavity would also be important in determining the amount of interreflection.

4.9 Conclusion

Current classification systems for wrinkles and microrelief in general are inadequate as a result of their qualitative nature and inherent problems with inter-user reproducibility. 3D in vivo profilometry provides objective analysis of skin microrelief and enables clinicians to predict and analyse the limitations and efficacy of various aesthetic procedures. The last decade has seen a shift toward 3D non invasive and in vivo measurements of skin roughness, however whilst numerous 3D techniques have been developed and used, none of them has been adopted as a standard. A photometric stereo based technique has been proposed for quantitative assessment of skin topography. Compared to other 3D imaging techniques it is economical, provides fast acquisition for everyday clinical usage and can easily recover skin colour and topographical information.

It is evident from the results that the BRDF of skin is not Lambertian in the visible part of the spectrum. The findings demonstrate that a lack of diffuse reflection when imaging using the green light and that a relativity diffuse behaviour exhibited under red light, adheres to the BRDF measurements produced by [95]. However, although there is no skin BRDF data for the blue part of the spectrum, the further decrease in depth of penetration and increase in absorption from 523nm to 462nm suggests a reduction of diffuse light reflection and increase in the specular

component. This variation in BRDF also explains the variation in shape estimation from each colour light at the concave parts of the skin and explains the over and under estimation of depth.

The use of white light for imaging skin using photometric stereo proved to be less effective than using light in the red part of the visible spectrum. Because white light is an aggregate of red, green and blue parts of the spectrum, the accuracy of the surface data obtained suffered due to the non-diffuse BRDF, especially at the green and blue parts of the visible spectrum.

Presented is a technique for minimising the effects of interreflection in skin with topographic features and varying reflectance and BRDF. Results, which were verified using ground truth data from a PRIMOS 4 device, show improvement in surface reconstruction for both light and dark skin subjects after using the proposed method in this research. The photometric stereo based 3D capture system has proved to be an efficient skin microrelief imaging device, it is low-cost and requires less acquisition and calibration time and also has a much larger field of view compared to other commercial skin microrelief imaging systems and can be used for *in vivo* measurement and quantitative analysis of skin relief.

Fractals and conventional 2D profile analysis were also performed on different wrinkle states for quantitative assessment. The fractal based technique provided

an added advantage over 2D roughness measurements by making use of complete 3D surface information and also did not require any high or low pass filtering. In the next chapter the experimental work will be extended by using polarizers to separate diffuse from specular reflection over the visible spectrum, in order to obtain more accurate skin topography.

Chapter 5

Shape from Polarisation

This chapter discusses the properties of skin when illuminated with polarised light with varying wavelengths. This chapter also discusses the Umov effect [115] for skin and an algorithm for improved shape recovery using photometric stereo by utilising polarisation information to separate specular and diffuse reflectance components of skin.

The majority of previous research using photometric stereo involves 3D reconstruction using both the diffuse and specular components, however this chapter focuses on the use of the specular component as it is the only form of light that comes directly off the surface without subsurface scattering or interreflections. This chapter discusses the interreflection problem for concave surfaces and uses polarisation based photometric stereo to minimise errors in recovered 3D shape. Also presented is a novel algorithm that makes use of specular highlights to im-

prove shape. The algorithm was first tested on synthetic images generated using PovRay®software and then it was applied to real world surfaces including human skin.

The following original contributions are discussed in this chapter:

- The Degree of polarisation increases as the reflectance of skin decreases in the visible spectrum.
- Darker skin reflects more polarised light than lighter skin for similar wavelength (λ).
- A novel algorithm to improve 3D shape recovery using polarisation based photometric stereo in the presence of interreflections and subsurface scattered light.

When only the diffuse component of light is used, the recovery of 3D skin shape gets better and better as the wavelength decreases towards the blue part of the spectrum from the red part. According to the interreflection theory for Shape from shading (SFS), the recovered shape improves at the concave region as the albedo of the surface decreases, however this thesis claims that there will still be a certain amount of error in recovered shape even with the decrease of albedo. Also, the specular reflected light must be used to improve shape as

it is the only form of light that comes directly of the surface without subsurface scattering or interreflections.

5.1 Literature Survey

A number of techniques have been used for combining polarisation information with photometric Stereo. Gary [116, 117], used Fresnel theory that relates the degree of polarisation of light with zenith angle and allows to calculate shape from diffuse polarisation. However this technique requires resolving a disambiguity in azimuth angle also the method requires capture of three images under 0,45, 90 degree orientation of polariser which increases the capture time and makes it less suitable for in vivo imaging of skin. Abhishek [118] used a multispectral light stage and polarised spherical gradient illumination to improve shape recovery of skin however their technique requires special arrangements of numerous light sources which makes it very expensive.

Most of the techniques based on photometric stereo alone assume specular highlights as outliers [2, 119, 120] and are usually removed to get more accurate shape. This approach does improve the overall shape, as the Lambertian assumption in photometric stereo fits more closely to the object reflectance after removal of specularities. However, this is only true for surfaces that are opaque

and are not concave and they are also limited by the assumption that a specular pixel cannot exist in more than one image which is not true for a variety of materials with wide specular lobes. The experiments conducted using polarisation based photometric stereo presented in this chapter suggest an increase in surface error if the specular highlights are ignored and also shows that for concave surfaces the specular reflected light is the only form of light that is purely reflected off the surface and leads to less error in 3D shape than the diffusely reflected light that contains subsurface scattered and interreflected light.

There are some techniques that make use of specular highlights to improve shape without using the polarisation information. A technique utilizing specular reflected light to recover fine scale details in a surface was proposed by [81]. Their method however involved capturing the object from hundreds of different light direction to acquire specular reflected light for each pixel. A more robust algorithm was proposed by Chung [121] that used both diffuse and specular reflected light to recover shape of rough surfaces by estimating the parameters of the Ward model. Georghiades [122] used the Torrance and Sparrow model with uncalibrated photometric stereo to recover both shape and reflectance properties of non Lambertian materials including human skin. However these methods cannot handle interreflections for concave shapes as both these techniques use diffuse compo-

nent along with specular highlights to recover 3D shape and the diffusely reflected light at concave surfaces come after multiple interreflections making it unsuitable for accurate recovery of 3D concave surfaces. This chapter describes the implementation of a novel polarisation based photometric stereo technique that makes use of specular highlights to improve shape at concave regions of the surface.

5.2 Polarisation Based Separation of Diffuse and Specular components

Most studies regarding improvement in shape recovery using photometric stereo have regarded specularities from surface reflections as noise and as such are removed as they do not fit into the Lambertian assumption used in the photometric stereo technique. This chapter explores the idea that specular reflection is the only form of light that has the least amount of noise in it, as it is directly reflected off the surface without interreflecting among surfaces and without any subsurface scattering. Also presented is a technique that makes use of specular highlights for accurate recovery of skin relief. The method uses polarisation information to separate diffuse from specularly reflected light and then uses an algorithm that incorporates the Torrance and Sparrow model with the measured BRDF of skin

to calculate shape from specular highlights.

The theory behind separating the diffuse from specular reflected light involves separation of photons based on their polarisation properties. Single and multiple scattered photons can be separated by capturing two images under the same lighting and viewing direction. This is done by altering the orientation of the polariser at the viewing point once parallel and perpendicular to the orientation of incident light polarisation. As the incident polarised light hits the tissue surface, the photons that are reflected from the superficial tissue layer retain their polarisation state while the photons that undergo multiple scattering within the tissue have a random polarisation state. The photons that are subject to multiple scattering events (diffuse light) are not suitable for photometric stereo based techniques, which assume that light is reflected from a single point without interacting with adjacent surfaces and subsurface layers of the material. The extent to which the light under analysis is polarised is given by degree of polarisation P

$$P = \frac{(I_{par} - I_{per})}{(I_{par} + I_{per})} = \frac{((S_u + 1/2M) - 1/2M)}{((S_u + 1/2M) + 1/2M)} = \frac{S_u}{(S_u + M)} \tag{5.1}$$

Where I_{par} is the image intensity captured with both the illumination and viewing polariser parallel to each other while I_{per} is the image intensity captured with

the illumination and viewing polariser perpendicular to each other. I_{par} image intensity has both the superficially reflected light S_u and half of the multiple scattered light M i.e. $(S_u + 1/2M)$ while the I_{per} image intensity only has half of the multiply scattered light i.e. $1/2M$.

5.3 Umov Effect

The Umov effect [115]suggests a decrease in the degree of polarisation of light due to multiple interparticle scattering for surfaces with higher albedo and also suggests an inverse relation between degree of polarisation P and the surface albedo shown in equation 5.2. This effect has been observed in different astronomical objects and small irregularly shaped particles [123]. This section investigates the Umov effect for different skin types, by analysing the variation in the degree of linear polarisation for wavelengths in the visible spectrum and for a range of phase angles.

$$P \propto \frac{1}{\alpha} \tag{5.2}$$

The value of P ranges between ± 1. Where a value of 0 represents unpolarised

light and ± 1 represents linearly polarised light. Highly reflective materials tend to reflect unpolarised light and darker surfaces reflect more polarised light. It is due to inter particle multiple scattering which decreases polarisation. Regarding humans, skin exhibits higher reflectance in the red part of the visible spectrum and decreases towards the blue part of the visible spectrum. To examine the variation of degree of polarisation with wavelength and skin types the following setup was used.

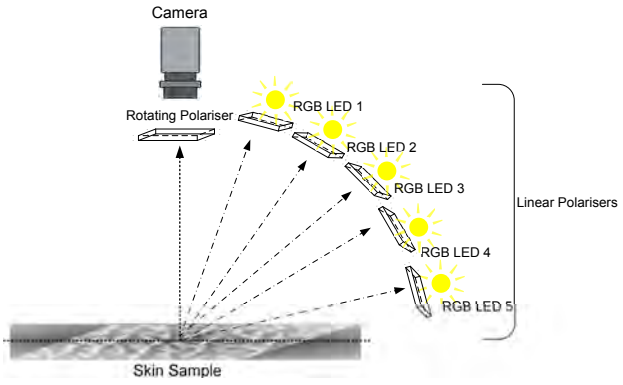

Figure 5.1: The setup uses a rotating polariser in front of the camera and linear polarisers in front of RGBW LEDs.

5.3.1 Setup for Umov Effect

For examining the Umov effect for skin the lights were arranged at varying slant angles of $31, 37, 42$ and 55 degrees as shown in Fig 5.1. The LED's used were 40 Watt RGBW(red,green,blue and white) LEDs[1] from LedEngin and an AVT Stingray F125B[2] camera. These LED's consist of a single emitter comprised

[1] For details of LED see datasheet in Appendix A
[2] Camera datasheet in Appendix A

of red, green, blue and white individually addressable dies. The dominant wavelength for each colour light was 462nm, 523nm and 625nm. Each LED had a linear polariser mounted in front of it and a rotating linear polariser in front of the camera. Also a Semrock FF01-457/530/628-23.3-D[3] triband filter was added to keep the spectral response of the LEDs to a relatively narrow range of wavelengths. The experiment was conducted on six subjects, among them three were Asians (Chinese) and the other three Caucasians (European).

Table 5.1: Variation of degree of polarisation with phase angle and wavelength for three Caucasian (European) subjects.

	Phase Angle(Deg)	Region	Degree of polarisation Red light	Green light	Blue light
Subject1	42	Forehead	0.1129	0.2359	0.2722
	42	Cheek	0.1226	0.2439	0.3074
	37	Forehead	0.1155	0.2282	0.2688
	37	Cheek	0.0829	0.1685	0.2025
	31	Forehead	0.1142	0.2373	0.2558
	31	Cheek	0.1256	0.2608	0.291
	55	Forehead	0.0696	0.1683	0.1496
	55	Cheek	0.1004	0.2257	0.2331
Subject2	42	Forehead	10.1044	0.1974	0.2455
	42	Cheek	0.1192	0.2667	0.3252
	37	Forehead	0.1242	0.2793	0.3258
	37	Cheek	0.0765	0.1563	0.1885
	31	Forehead	0.1188	0.219	0.2702
	31	Cheek	0.1065	0.2252	0.2798
	55	Forehead	0.053	0.144	0.1624
	55	Cheek	0.0521	0.0988	0.1727
Subject3	42	Forehead	0.0794	0.171	0.2265
	42	Cheek	0.0522	0.1282	0.1825
	37	Forehead	0.0651	0.1425	0.1648
	37	Cheek	0.0194	0.0399	0.0664
	31	Forehead	0.1081	0.2132	0.2793
	31	Cheek	0.0297	0.0966	0.1183
	55	Forehead	0.0367	0.08	0.1374
	55	Cheek	0.0195	0.0012	0.0631

[3]For details of filter see datasheet in Appendix A

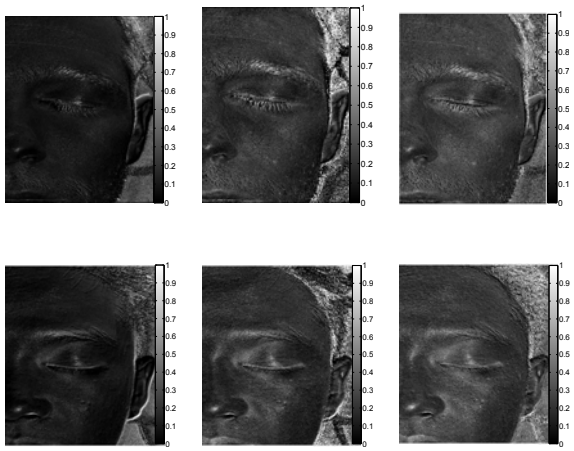

Figure 5.2: 1st row: Degree of polarisation (DOP) for red light, green and blue light for a Caucasian (European) Subject. 2nd row: Degree of polarisation for red light, green and blue light for a Asian (Chinese) Subject. (The Image intensity represents the degree of polarisation of light in the range 0 to 1)

Table 5.2: Variation of degree of polarisation with phase angle and wavelength for three Asian (Chinese) subjects.

	Phase Angle(Deg)	Region	Degree of polarisation Red light	Green light	Blue light
Subject1	42	Forehead	0.1273	0.2292	0.2898
	42	Cheek	0.1416	0.2704	0.328
	37	Forehead	0.1329	0.2365	0.2972
	37	Cheek	0.078	0.1506	0.1949
	31	Forehead	0.1099	0.2079	0.2707
	31	Cheek	0.1225	0.2466	0.2912
	55	Forehead	0.0741	0.1334	0.276
	55	Cheek	0.1225	0.1724	0.2123
Subject2	42	Forehead	0.137	0.2766	0.3491
	42	Cheek	0.1601	0.3228	0.3986
	37	Forehead	0.1358	0.2538	0.3197
	37	Cheek	0.0572	0.1331	0.16692
	31	Forehead	0.1358	0.2926	0.3519
	31	Cheek	0.1022	0.1331	0.2869
	55	Forehead	0.0919	0.1755	0.2568
	55	Cheek	0.059	0.1567	0.21
Subject3	42	Forehead	0.15	0.3038	0.3744
	42	Cheek	0.1548	0.3189	0.3925
	37	Forehead	0.1292	0.2473	0.3151
	37	Cheek	0.1425	0.2594	0.3023
	31	Forehead	0.1955	0.3691	0.4392
	31	Cheek	0.1597	0.3162	0.3721
	55	Forehead	0.0842	0.1925	0.2445
	55	Cheek	0.0885	0.2091	0.2342

The degree of polarisation was measured for Caucasian and Asian skin types and their variation over cheek and forehead regions is presented in table 5.1 and 5.2 respectively. The measurements show that the degree of polarisation increases with decrease in wavelength in the visible spectrum for a particular skin type.

The degree of polarisation when averaged over the whole face was also higher for darker skin than lighter skin and it also increased with decrease in surface albedo due to change in wavelength in the visible spectrum shown in Fig 5.2. These effects in human skin have not been investigated before and are new additions to the current state-of-the-art of skin optics.

5.4 Shape from Specular and Diffuse Reflection

This section explains a novel algorithm for improving photometric stereo based shape recovery using polarisation information. The data obtained from polarisation imaging consists of diffuse only images, diffuse+specular images and specular only images. Fig. 5.4 shows one such dataset obtained for skin using polarisation. The imaging setup consisted of four LEDs with linear polarisers mounted on each one of them and a camera with a rotating polariser in front as shown in Fig. 5.3. In order to test the algorithm, synthetic surfaces were generated using

PovRay software that mimic similar characteristics as that obtained using polarisation. Experiments were then conducted on real world materials by creating a concave shape in Plasticine material to simulate the effects of interreflections and by using the proposed algorithm to minimise its effects. Finally the algorithm was tested on human skin by using the measured BRDF of skin from the Mitsubishi Electric Research Laboratories (MERL) database [124].

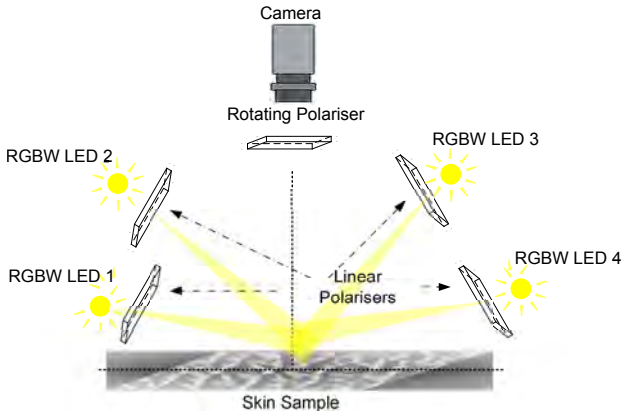

Figure 5.3: The four light photometric setup uses a rotating polariser in front of the camera and four linear polarisers in front of RGBW LEDs.

5.5 Synthetic Image Analysis

The algorithm was first tested on a synthetic shape modelled using Phong reflectance model. The images synthesised were similar to those obtained from polarisation based imaging i.e. diffuse reflectance of the object, specular reflectance and the combined diffuse and specular reflectance. Fig 5.5 shows the synthesised images using the Phong model.

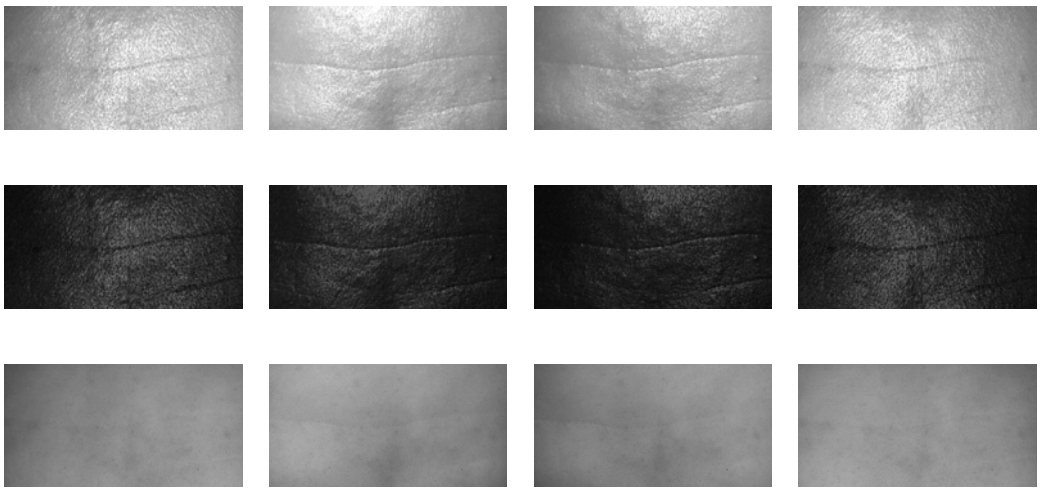

Figure 5.4: (a)Skin images obtained using polarisation. 1st row: Images containing diffuse+specular component of reflected light, Second row: Images containing specular reflection component only, Third row: Images containing diffuse component only.

The algorithm works by first creating a search space for each point in the image. For each point, the set of normals from the searchspace are used to find the correct normal by reconstructing the original images using the Phong model. The search space is created by using two types of images, one with both the diffuse and specular (I_{ds}) component, and one with diffuse component only (I_d). A set of normals is calculated using the basic Lambertian photometric stereo from each I_{ds} and I_d. The images containing both the diffuse and specular component provides the upperbound on serach for normals as it contains the overestimated slant angles due to specularities, while the images containing the diffuse component only provide the lowerbound in search space as they contain the underestimated slants due to interreflections. The ideal surface normal lies somewhere between

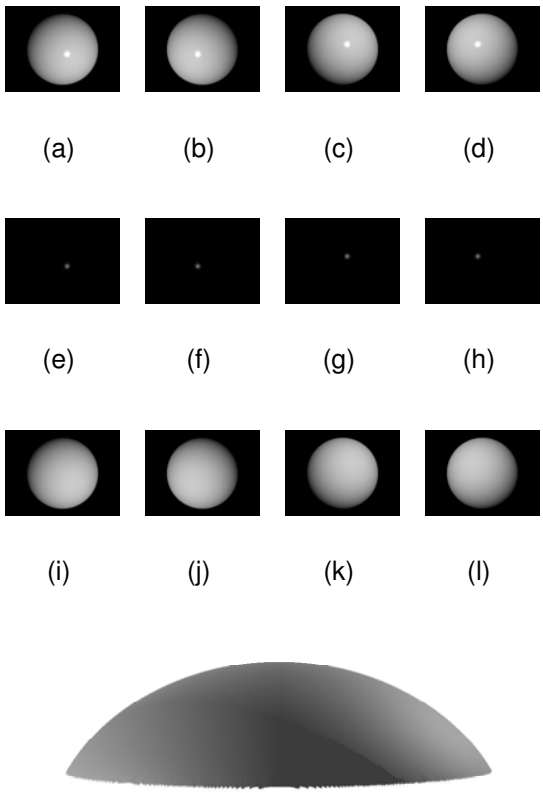

Figure 5.5: (a)-(l)A Synthesised ball using Phong model for validation of proposed search space. Top row: ball illuminated from four light directions with both specular and diffuse component. 2nd row: using specular component only. 3rd row: using diffuse component only. (m) 3D shape recovered using proposed algorithm.

the upper and lower bounds set by these two set of images. Fig 5.6 shows the graphical representation of this searchspace. Fig. 5.5(m) shows the recovered shape of sphere using this search space and the proposed algorithm explained in section 5.6.

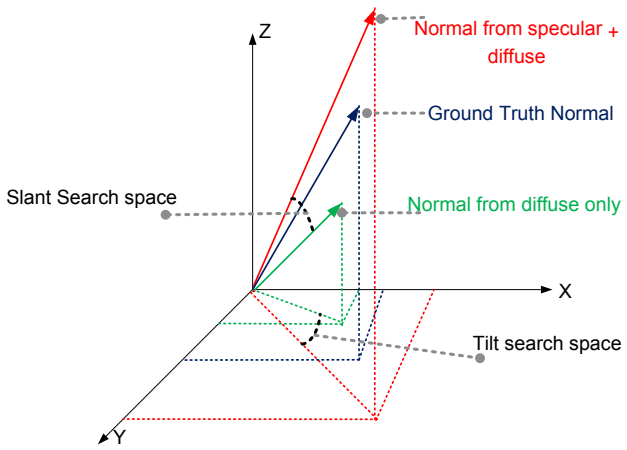

Figure 5.6: The Slant tilt search space.

5.6 Algorithm

The following steps describe the proposed algorithm.

1. Calculate pseudo surface normals using Specular + diffuse light (using Lambertian model).

2. Calculate pseudo surface normals using diffuse light only (using Lambertian model).

3. Generate the slant and tilt search space for each pixel using 1 and 2.

4. For each pixel, pick the maximum specular intensity from all images and corresponding light direction.

5. Create a lookup table using the corresponding reflectance model.

6. From the look up table and by using the above search space, calculate: $min[(I_{Image_S} - I_{Model_S})^2]$ where I_{Model_S} is the specular component calculated

using the corresponding model and I_{Image_S} is the specular component obtained from polarisation based image.

5.7 Real Surface Analysis

The proposed technique was then applied to real images of plasticine. First concave grove of 60 degree was created in the Plasticine mould. As the angles between the two facing patches were set to 60 degrees, by measuring the angle between the normals on each plane we can find the angle between the two planes. This was done by taking the dot product of normals.

$$A = cos^{-1}(\frac{(S.R)}{|S||R|}) \tag{5.3}$$

As discussed before the data from polarisation can be categorised into diffuse only (I_D), diffuse+specular (I_{DS}) , specular only (I_S). Using the same algorithm the slant and tilt search space was created using the Lambertian model. However, the function was minimised by using both the diffuse and specular components of the Ward model. The Ward reflectance model does not account for interreflections and hence the recovered angle between two planes contained a RMS error

of 4.28 degrees, which is still better than a RMS error of 9.6 degrees when recovered using the basic Lambertian model. A greater improvement can be seen by using the specular only component of the image I_{Image_S} while solving the following for each pixel using Eq. 5.4, resulting in a RMS error of only 2.89 degrees. This validated the claim that the specular reflected light is more suited to surface reconstruction using photometric stereo and the diffusely reflected light will always result in inaccurate shape recovery when the surface under consideration is concave.

$$min[(I_{Image_S} - I_{Ward_S})^2] \tag{5.4}$$

Where I_{Ward_S} is the specular component generated from Ward model using the normals in the search space shown in Fig 5.6. The Ward reflectance model is given by:

$$f_r(\omega_o, \omega_i) = \frac{\rho_d}{\pi} + \rho_s \frac{1}{\sqrt{\cos\theta_i \cos\theta_o}} \frac{exp\left(-\frac{\tan^2\varphi}{\sigma^2}\right)}{4\pi\sigma^2}. \tag{5.5}$$

ω_o, ω_i are the incident and reflected radiance. ρ_d and ρ_s are the diffuse and specular coefficients respectively, σ is the roughness coefficient that determines the size of specular lobe and φ is the angle between the surface normal and the halfway vector.

5.8 Skin Microrelief Analysis

After testing the algorithm on synthetic shapes and on Plasticine material, the experiments were extended to human skin. The MERL database contains the Torrance and Sparrow model parameters for different skin types, age groups and gender. These parameters were used in conjunction with the proposed algorithm to improve the recovered 3D skin shape using polarisation based photometric stereo. The physically based Torrance and Sparrow model defined in 5.6 was used.

$$f_s = \rho_s * \frac{1}{\pi} * \frac{FDG}{(\vec{N} \cdot \vec{V})(\vec{N} \cdot L)} \tag{5.6}$$

It is a microfacet based model, where the term D defines the microfacet orientation distribution for the Halfway vector and determines the overall roughness of the surface. The term F is the Fresnel reflection coefficient and the the term G (geometric attenuation factor) handles the shadowing and masking of the microfacets and calculates the resulting amount of light remaining after these effects. Its value ranges between 0 to 1 for completely shadowed(0) to no shadowing(1).

For the microfacet orientation distribution D the Beckman distribution was

used, defined in 5.7.

$$D = \frac{1}{m^2 \cos^4 \alpha} e^{-(\tan \alpha / m)^2} \tag{5.7}$$

α is the angle between $\vec{N}$ and $\vec{H}$ and m is the root mean square slope of the microfacets. For small values of m the reflection becomes highly directional while for higher values of m the reflection is more spread out.

The geometric attenuation factor is given by:

$$G = \min \left\{ 1, \frac{2(\vec{N} \cdot \vec{H})(\vec{N} \cdot \vec{V})}{(\vec{V} \cdot \vec{H})}, \frac{2(\vec{N} \cdot \vec{H})(\vec{N} \cdot \vec{L})}{(\vec{V} \cdot \vec{H})} \right\} \tag{5.8}$$

$$G_1 = \frac{2(\vec{N} \cdot \vec{H})(\vec{N} \cdot \vec{V})}{(\vec{V} \cdot \vec{H})} \tag{5.9}$$

$$G_2 = \frac{2(\vec{N} \cdot \vec{H})(\vec{N} \cdot \vec{L})}{(\vec{V} \cdot \vec{H})} \tag{5.10}$$

Where 5.9 is the light blocked from the viewer and 5.10 is for light in shadow.

The Fresnel equation describes the ratio for reflected light as:

$$F = \frac{1}{2} * (\frac{\sin^2(\phi - \theta)}{\sin^2(\phi + \theta)} + \frac{\tan^2(\phi - \theta)}{\tan^2(\phi - \theta)}) \tag{5.11}$$

or the Fresnel term can be written as:

$$F = \frac{1}{2}\frac{(g-c)^2}{(g+c)^2}(1 + \frac{[c(g+c)-1]^2}{[c(g-c)-1]^2}) \tag{5.12}$$

where $c = \cos(\phi) = \vec{L} \cdot \vec{H}$, η is the index of refraction and $g^2 = \eta^2 + c^2 - 1$.

Fig. 5.7 shows the effect of using the specular component to improve 3D geometry recovered using photometric stereo. The experiments were conducted on the forehead region of Caucasian and Asian skin types and using the algorithm, while the parameters for the Torrance and Sparrow model used in the algorithm were taken from the MERL database. The results show that the diffusely reflected light contains subsurface scattered and interreflected light which result in a smoother 3D skin geometry and loses the high frequency information such as wrinkles as shown in Fig. 5.7(b) and 5.7(e) for Caucasian and Asian Skin types respectively, however the specular component of reflected light did reveal more fine details of the skin as shown in Fig. 5.7(c) and 5.7(f).

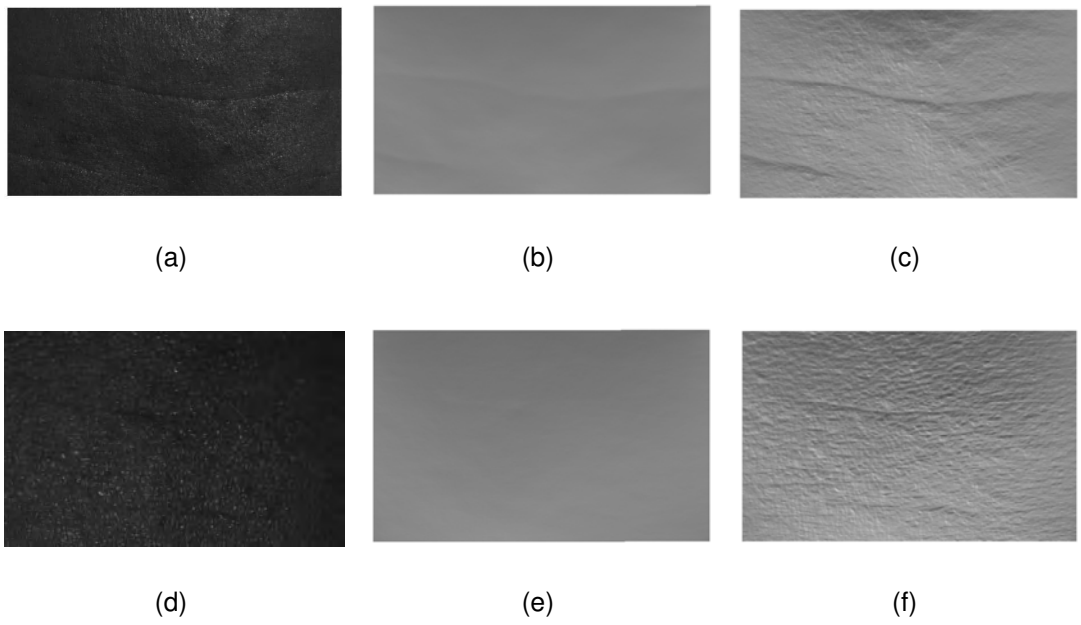

Figure 5.7: (a)One of the captured images of Caucasian subject (b) 3D reconstruction using diffuse component only (c) 3D reconstruction from the proposed algorithm. (d) One of the captured images of Asian subject (e) 3D reconstruction using diffuse component only (f) 3D reconstruction using the proposed algorithm.

5.9 Discussion

This chapter introduced a method for the improvement in 3D shape recovery using polarisation based photometric stereo. The results clearly show that the diffusely reflected light is not always the best form of reflected light for accurate 3D shape recovery using photometric stereo, especially when the surface is concave and translucent. The results from the algorithm were first validated using synthetic data and then on a Plasticine material with a concave groove in it. The results clearly show improvement in surface slant angles when the specular reflected light was used in conjunction with the proposed algorithm and again when

later applied on human skin. The experiments on the Umov effect in skin also adds to current state of the art by suggesting a increase in degree of polarisation for darker skin compared to lighter skin and also showed that the decrease in skin reflectance within the visible spectrum from red towards the blue light also results in increase in polarised light reflection, these effects were both seen in Caucasian and Asian skin types.

Chapter 6

Conclusions, Limitations and Future Work

The following is a summary of contributions arising from this work.

6.1 Summary of Contributions

- The interreflection phenomenon in general is a known problem - with the exception of human skin. There is no published work that has looked into interreflections in the (in-vivo) analysis of human skin, using photometric stereo, for different skin types and where there is a difference in reflectance for each skin type as well as a difference in BRDF. The findings presented in this thesis shows that the interreflections within concave parts of the skin (wrinkles) are dependent on the reflectance of the skin. What makes this

interesting is that skin exhibits a different reflectance at different wavelength bands (red, green, blue) and that in addition there is difference in the BRDF at these bands. Moreover, the traditional theory of interreflection cannot be directly applied to skin. If this were applicable to skin, we would have seen more accurate shape recovery by just using blue light (where the reflectance of skin is lowest). Also the skin BRDF is not Lambertian for these colored lights and instead of underestimating the concave shape, blue light actually overestimates the concave shape 4.10(d), which is unusual and is not consistent with the traditional theory of interreflection. The finding that interreflections in skin are not only dependent on reflectance but also on the BRDF is novel and cannot be derived from the state of the art.

The inter-reflection problem has been addressed previously but not in the case of human skin. Most previous methods, that have tackled inter-reflections, are limited to opaque materials that have a close Lambertian BRDF

- To the best of author's knowledge, no published work has so far looked into the quantitative assessment of 3D skin microrelief using photometric stereo. Much of the analysis concerning the accuracy of skin microrelief is visually qualitative. The skin topography measurements presented in this thesis were validated using the PRIMOS 4 device and detailed experiments

were performed with different skin types to determine the amount of error in surface normals and reconstructed height for each individual color (R, G, B) and white light caused by differences in BRDF.

- Earlier work regarding the surface accuracy analysis between infrared and white light showed that infrared light was superior in capturing accurate skin topography to white light [5]. This thesis further contributes to the state-of the-art by explaining the reasons for inaccurate acquisition of skin topography while using white light.

- The finding that the BRDF of skin varies with wavelength in the visible spectrum and that it also varies with different skin types.

- The development of a new technique for minimising surface errors due to interreflection in the presence of wrinkles (using variation in spectral gradients). Since most methods developed for handling interreflection are limited to surfaces with a Lambertian BRDF, a new method was developed for skin as the BRDF of skin is not Lambertian.

- A novel algorithm for interreflection minimisation using segmentation based method.

- The finding that human skin reflects more polarised light as the reflectance

decreases (in visible spectrum) and darker skin exhibits a higher degree of polarisation than lighter skin at similar wavelengths in the visible spectrum (The Umov effect for skin). These effects in human skin have not been investigated before and are new additions to the current state-of-the-art of skin optics.

- A novel algorithm for shape from specular reflection using Polarisation. (Verified using simulated and real data)

In summary this thesis discusses the interreflection phenomenon in human skin for wavelengths in the visible spectrum. Novel algorithms were implemented to improve the recovered 3D skin topography in the presence of interreflections. The results show that there is a difference in BRDF for all skin types and there is a difference in the amount of polarised reflected light for all skin types at similar wavelengths in the visible spectrum. A novel polarimetric photometric stereo based technique is also presented to minimise the errors in 3D recovered shape due to interreflections, the proposed algorithm also demonstrates that the diffusely reflected light is not best suited for shape recovery of concave surfaces.

6.2 Future Work

The techniques proposed in this thesis using color and polarisation information with photometric stereo can be modified to work with wounds, scars and lesion information, however that would require a detailed understanding of the spectral BRDF of normal and affected human skin. The problem is somewhat more complex in the case of wounds and scars, as they have different color and composition compared to the normal surrounding skin. The proposed algorithms were verified by simulating complex BRDF, similar could be done in case of wounds and scars analysis by creating synthetic shapes with varying color and BRDF from the surroundings.

The Umov effect showed a variation in the content of specular and diffusely reflected light for different skin types and with varying wavelength. The variation suggests a difference in polarised BRDF as well for wavelengths in the visible spectrum however there are currently no data sets available that show the polarimetric BRDF measurements for different skin types at varying wavelengths. These measurements are difficult to obtain specially for skin due to low acquisition speed of current systems for full BRDF measurement. Hence further research is required on novel methods for polarimetric BRDF measurements of skin.

The MERL BRDF data set is the only one available for different skin types

however it was only calculated for white light only. The availability of multispectral skin BRDF data is scarce, as most measurements are taken using white light for a limited set of incoming and outgoing angles. There are currently no datasets that show dense BRDF measurements for different types of skin, over a range of wavelengths. Knowledge of skin BRDF is not only important for realistic skin renderings but also for accurate 3D reconstruction of skin, as shape from shading algorithms are dependent on how light is reflected from the surface and how light distribution varies as a function of wavelength. The future work should focus on dense multispectral BRDF measurements for all skin types.

REFERENCES

[1] L. I. M. J. Vrhel, R. Gershon, "Measurement and analysis of object reflectance spectra," Color Research and Application **19**, 4–9 (1994).

[2] J. Sun, M. Smith, L. Smith, S. Midha, and J. Bamber, "Object surface recovery using a multi-light photometric stereo technique for non-Lambertian surfaces subject to shadows and specularities," Image and Vision Computing **25**, 1050–1057 (2007).

[3] S. K. Nayar, K. Ikeuchi, and T. Kanade, "Shape from interreflections," International Journal of Computer Vision **6**, 173–195 (1991).

[4] M. Liao, X. Huang, and R. Yang, "Interreflection removal for photometric stereo by using spectrum-dependent albedo," Computer Vision and Pattern Recognition pp. 689–696 (2011).

[5] M. F. Hansen, G. a. Atkinson, L. N. Smith, and M. L. Smith, "3D face re-

constructions from photometric stereo using near infrared and visible light," Computer Vision and Image Understanding **114**, 942–951 (2010).

[6] A. Bayat, "Skin scarring," British Medical Journal **326**, 88 (2003).

[7] "2009 report of the 2008 statistics, National Clearing House of Plastic Surgery, American Society of Plastic Surgeons," Tech. rep., American Society of Plastic Surgeons (2009).

[8] "Industry profile: Skincare in Europe," in "Reference Code: 0201-0708," (Datamonitor, July 2010, 2010), July.

[9] D. J. Day, C. M. Littler, R. W. Swift, and S. Gottlieb, "The wrinkle severity rating scale: a validation study," American journal of clinical dermatology **5**, 49–52 (2004).

[10] K. Hashimoto, "New methods for surface ultrastructure: comparative studies of scanning electron microscopy, transmission electron microscopy and replica method," International Journal of Dermatology **13**, 357–381 (1974).

[11] T. Lee, L. Tchvialeva, H. Zeng, D. McLean, and H. Lui, "Laser speckle and skin cancer: skin roughness assessment," in "Proceedings of SPIE," , vol. 7388 (2009), vol. 7388, p. 738816.

[12] J. Lévêque, “EEMCO guidance for the assessment of skin topography,” Journal of the European Academy of Dermatology and Venereology **12**, 103–114 (1999).

[13] S. K. Chang, D. Arifler, R. Drezek, M. Follen, and R. Richards-Kortum, “Analytical model to describe fluorescence spectra of normal and preneoplastic epithelial tissue: comparison with Monte Carlo simulations and clinical measurements,” Journal of biomedical optics **9**, 511–22 (2004).

[14] B. J. Tromberg, L. O. Svaasand, M. K. Fehr, S. J. Madsen, P. Wyss, B. Sansone, and Y. Tadir, “A mathematical model for light dosimetry in photodynamic destruction of human endometrium,” Physics in medicine and biology **41**, 223–37 (1996).

[15] S.-H. Tseng, P. Bargo, A. Durkin, and N. Kollias, “Chromophore concentrations, absorption and scattering properties of human skin in-vivo,” Optics express **17**, 14599–617 (2009).

[16] T. L. Troy and S. N. Thennadil, “Optical properties of human skin in the near infrared wavelength range of 1000 to 2200 nm,” Journal of biomedical optics **6**, 167–76 (2001).

[17] G. Zonios and A. Dimou, “Modeling diffuse reflectance from semi-infinite

turbid media: application to the study of skin optical properties," Optics express **14**, 8661–74 (2006).

[18] C. Simpson, M. Kohl, M. Essenpreis, and M. Cope, "Near-infrared optical properties of ex vivo human skin and subcutaneous tissues measured using the Monte Carlo inversion technique," Physics in Medicine and Biology **43**, 2465 (1998).

[19] K. Tsukahara, K. Sugata, O. Osanai, A. Ohuchi, Y. Miyauchi, M. Takizawa, M. Hotta, and T. Kitahara, "Comparison of age-related changes in facial wrinkles and sagging in the skin of Japanese, Chinese and Thai women," Journal of dermatological science **47**, 19–28 (2007).

[20] G. D. Monheit, E. C. Gendler, B. Poff, L. Fleming, N. Bachtell, E. Garcia, and D. Burkholder, "Development and validation of a 6-point grading scale in patients undergoing correction of nasolabial folds with a collagen implant," Dermatologic surgery **36**, 1809–1816 (2010).

[21] A. Carruthers, J. Carruthers, B. Hardas, M. Kaur, R. Goertelmeyer, D. Jones, B. Rzany, J. Cohen, M. Kerscher, T. C. Flynn, C. Maas, G. Sattler, A. Gebauer, R. Pooth, K. McClure, U. Simone-Korbel, and L. Buchner, "A

validated lip fullness grading scale," Dermatologic Surgery **34**, S161–S166 (2008).

[22] J. S. Ryu, S. G. Park, T. J. Kwak, M. Y. Chang, M. E. Park, K. H. Choi, K. H. Sung, H. J. Shin, C. K. Lee, Y. S. Kang, M. S. Yoon, M. J. Rang, and S. J. Kim, "Improving lip wrinkles: lipstick related image analysis," Skin research and technology **11**, 157–64 (2005).

[23] A. Carruthers, J. Carruthers, B. Hardas, M. Kaur, R. Goertelmeyer, D. Jones, B. Rzany, J. Cohen, M. Kerscher, T. C. Flynn, C. Maas, G. Sattler, A. Gebauer, R. Pooth, K. McClure, U. Simone-Korbel, and L. Buchner, "A validated grading scale for marionette lines," Dermatologic surgery **34 Suppl 2**, S167–S172 (2008).

[24] A. Carruthers, J. Carruthers, B. Hardas, M. Kaur, R. Goertelmeyer, D. Jones, B. Rzany, J. Cohen, M. Kerscher, T. C. Flynn, C. Maas, G. Sattler, A. Gebauer, R. Pooth, K. McClure, U. Simone-Korbel, and L. Buchner, "A validated grading scale for forehead lines," American Society for Dermatologic Surgery **34**, S155–S160 (2008).

[25] G. Lemperle, R. Holmes, S. Cohen, and S. Lemperle, "A classification of facial wrinkles," Plastic and reconstructive surgery **108**, 1735 (2001).

[26] J. Chung, S. Lee, C. Youn, B. Park, K. Kim, K. Park, K. Cho, and H. Eun, "Cutaneous photodamage in Koreans: influence of sex, sun exposure, smoking, and skin color," Archives of dermatology **137**, 1043–1051 (2001).

[27] R. S. Narins, F. Brandt, J. Leyden, Z. P. Lorenc, M. Rubin, and S. Smith, "A randomized, double-blind, multicenter comparison of the efficacy and tolerability of Restylane versus Zyplast for the correction of nasolabial folds," Dermatologic surgery **29**, 588–595 (2003).

[28] S. H. Goh, "The treatment of visible signs of senescence: the Asian experience," The British journal of dermatology **122 Suppl**, 105–109 (1990).

[29] U. P. Kappes, "Skin ageing and wrinkles: clinical and photographic scoring." Journal of cosmetic dermatology **3**, 23–5 (2004).

[30] H. C. Eun, "Cutaneous photodamage in Asians." The Journal of dermatology **28**, 614–6 (2001).

[31] D. SHOSHANI, "The modified Fitzpatrick Wrinkle Scale: a clinical validated measurement tool for nasolabial wrinkle severity assessment," Dermatologic . . . pp. S85–S91 (2008).

[32] A. Vierkötter, T. Schikowski, U. Ranft, D. Sugiri, M. Matsui, U. Krämer, and

J. Krutmann, “Airborne Particle Exposure and Extrinsic Skin Aging,” The Journal of investigative dermatology pp. 2719–2726 (2010).

[33] R. G. Glogau, “Aesthetic and anatomic analysis of the aging skin,” Seminars in cutaneous medicine and surgery **15**, 134–138 (1996).

[34] L. Fritschi, D. Battistutta, G. M. Strutton, and A. Green, “A non-invasive measure of photoageing,” International journal of epidemiology **24**, 150–154 (1995).

[35] K. Tsukahara, M. Hotta, O. Osanai, T. Fujimura, T. Kitahara, and Y. Takema, “The effect of eye opening and closing on the result of facial wrinkle assessment,” Skin research and technology **15**, 384–391 (2009).

[36] T. Fujimura, K. Sugata, K. Haketa, and M. Hotta, “Roughness analysis of the skin as a secondary evaluation criterion in addition to visual scoring is sufficient to evaluate ethnic differences in wrinkles,” International journal of cosmetic science **31**, 361–7 (2009).

[37] C. Larnier, J. P. Ortonne, A. Venot, B. Faivre, J. C. Béani, P. Thomas, T. C. Brown, and E. Sendagorta, “Evaluation of cutaneous photodamage using a photographic scale,” The British journal of dermatology **130**, 167–73 (1994).

[38] M. C. T. Bloemen, M. S. van Gerven, M. B. a. van der Wal, P. D. H. M. Verhaegen, and E. Middelkoop, “An objective device for measuring surface roughness of skin and scars,” Journal of the American Academy of Dermatology **64**, 706–15 (2011).

[39] T. Fujimura, K. Haketa, M. Hotta, and T. Kitahara, “Global and systematic demonstration for the practical usage of a direct in vivo measurement system to evaluate wrinkles,” International journal of cosmetic science **29**, 423–436 (2007).

[40] J. Leveque and B. Querleux, “SkinChip, a new tool for investigating the skin surface in vivo,” Skin research and technology **9**, 343–347 (2003).

[41] K. De Paepe, J. M. Lagarde, Y. Gall, D. Roseeuw, and V. Rogiers, “Microrelief of the skin using a light transmission method,” Archives of dermatological research **292**, 500–10 (2000).

[42] J. L. Levy, J.-J. Servant, and E. Jouve, “Botulinum toxin A: a 9-month clinical and 3D in vivo profilometric crow’s feet wrinkle formation study,” Journal of cosmetic and laser therapy **6**, 16–20 (2004).

[43] J. Lagarde, C. Rouvrais, D. Black, S. Diridollou, and Y. Gall, “Skin topogra-

phy measurement by interference fringe projection: a technical validation," Skin Research and Technology **7**, 112–121 (2001).

[44] W. Manuskiatti, D. Triwongwaranat, S. Varothai, S. Eimpunth, and R. Wanitphakdeedecha, "Efficacy and safety of a carbon-dioxide ablative fractional resurfacing device for treatment of atrophic acne scars in Asians," Journal of the American Academy of Dermatology **63**, 274–283 (2010).

[45] S. Laube, S. Taibjee, and S. W. Lanigan, "Treatment of resistant port wine stains with the V Beam pulsed dye laser," Lasers in surgery and medicine **33**, 282–287 (2003).

[46] T. Cook, "Profilometry of skina useful tool for the substantiation of cosmetic efficacy," J Soc Cosmet Chem **31**, 339–359 (1980).

[47] S. Makki, J. Barbene, and P. Agache, "A quantitative method for the assessment of the microtopography of human skin," Acta Dermatovener **59**, 285–291 (1979).

[48] I. Sarkany, "A method for studying the microtopography of the skin." British Journal of Dermatology **74**, 254–259 (1962).

[49] C. Garber and C. Nightingale, "Characterizing cosmetic effects and skin

morphology by scanning electron microscopy," J Soc Cosmet Chem **27**, 509–531 (1976).

[50] K. De Paepe, J. M. Lagarde, Y. Gall, D. Roseeuw, and V. Rogiers, "Microrelief of the skin using a light transmission method," Archives of dermatological research **292**, 500–510 (2000).

[51] S. Akazaki, H. Nakagawa, H. Kazama, O. Osanai, M. Kawai, Y. Takema, and G. Imokawa, "Age-related changes in skin wrinkles assessed by a novel three-dimensional morphometric analysis," British Journal of Dermatology **147**, 689–695 (2002).

[52] C. Edwards, R. Heggie, and R. Marks, "A study of differences in surface roughness between sun-exposed and unexposed skin with age," Photodermatology, photoimmunology & photomedicine **19**, 169–74 (2003).

[53] S. Jaspers, "Rapid in vivo measurement of the topography of human skin by active image triangulation using a digital micromirror device," Skin Research and Technology **30**, 129–207 (1999).

[54] P. M. Friedman, G. R. Skover, G. Payonk, A. N. B. Kauvar, and R. G. Geronemus, "3D in-vivo optical skin imaging for topographical quantitative

assessment of non-ablative laser technology." American Society for Dermatologic Surgery **28**, 199–204 (2002).

[55] H. K. Lee, Y. K. Seo, J. H. Baek, and J. S. Koh, "Comparison between ultrasonography (Dermascan C version 3) and transparency profilometry (Skin Visiometer SV600)," Skin research and technology **14**, 8–12 (2008).

[56] R. J. WOODHAM, "Photometric stereo: A reflectance map technique for determining surface orientation from image intensity," in "Proceedings of the Society of Photo-Optical Instrumentation Engineers Conference on Image Understanding Systems and Industrial Applications," (1978), pp. 136–143.

[57] J. Sun, M. Smith, L. Smith, L. Coutts, R. Dabis, C. Harland, and J. Bamber, "Reflectance of human skin using colour photometric stereo: with particular application to pigmented lesion analysis," Skin research and technology **14**, 173–179 (2008).

[58] Y. Ding, L. Smith, M. Smith, J. Sun, and R. Warr, "Obtaining malignant melanoma indicators through statistical analysis of 3D skin surface disruptions," Skin research and technology **15**, 262–270 (2009).

[59] Y. Zhou, M. Smith, L. Smith, A. Farooq, and R. Warr, "Enhanced 3D curva-

ture pattern and melanoma diagnosis," Computerized medical imaging and graphics **35**, 155–165 (2011).

[60] M. Smith and L. Smith, "Infra-red photometric stereo," (2004).

[61] a. Farooq, M. Smith, L. Smith, and S. Midha, "Dynamic photometric stereo for on line quality control of ceramic tiles," Computers in Industry **56**, 918–934 (2005).

[62] J. Yamada, A. Kawamura, Y. Miura, S. Takata, and K. Ogawa, "Study on radiation transfer in human skin for cosmetics," Journal of Quantitative Spectroscopy and Radiative Transfer **93**, 219–230 (2005).

[63] M. Setaro and A. Sparavigna, "Irregularity skin index (ISI): a tool to evaluate skin surface texture," Skin Research and Technology **7**, 159–163 (2001).

[64] M. Egawa, M. Oguri, T. Kuwahara, and M. Takahashi, "Effect of exposure of human skin to a dry environment," Skin Research and Technology **8**, 212–218 (2002).

[65] U. Jacobi, M. Chen, G. Frankowski, R. Sinkgraven, M. Hund, B. Rzany, W. Sterry, and J. Lademann, "In vivo determination of skin surface topography using an optical 3D device," Skin research and technology **10**, 207–214 (2004).

[66] J. C. Barbenel, S. Makki, and P. Agache, “The variability of skin surface contours,” Annals of biomedical engineering **8**, 175–182 (1980).

[67] K. Articus, C. Brown, and K. Wilhelm, “Scale-sensitive fractal analysis using the patchwork method for the assessment of skin roughness,” Skin Research and Technology **7**, 164–167 (2001).

[68] F. Blateyron, “New 3D parameters and filtration techniques for surface metrology,” Proceeding of JSPE Annual Congress2006 (2006).

[69] R. Cook and K. Torrance, “A reflectance model for computer graphics,” ACM Transactions on Graphics (TOG) **1**, 7–24 (1982).

[70] C. Schlick, “An Inexpensive BRDF Model for Physicallyâbased Rendering,” Computer graphics forum (1994).

[71] A. Spizzichino and P. Beckmann, *The Scattering of Electromagnetic Waves from Rough Surfaces* (New York, Paris, 1963).

[72] G. Ward, “Measuring and modeling anisotropic reflection,” ACM SIGGRAPH Computer Graphics pp. 265–272 (1992).

[73] M. L. Smith and L. N. Smith, “Dynamic photometric stereoa new technique for moving surface analysis,” Image and Vision Computing **23**, 841–852 (2005).

[74] M. Chandraker and F. Kahl, “Reflections on the generalized bas-relief ambiguity,” in “Computer Vision and Pattern Recognition,” , vol. 1 (IEEE, 2005), vol. 1, pp. 788–795.

[75] A. Yuille and D. Snow, “Determining generative models of objects under varying illumination: Shape and albedo from multiple images using SVD and integrability,” International Journal of . . . **35**, 203–222 (1999).

[76] D. Forsyth and A. Zisserman, “Mutual illumination,” Proceedings CVPR ’89: IEEE Computer Society Conference on Computer Vision and Pattern Recognition pp. 466–473 (1989).

[77] T. Yamada, H. Saito, and S. Ozawa, “3d reconstruction of skin surface from image sequence,” in “IAPR Workshop on Machine Vision . . . ,” (1998), pp. 3–6.

[78] A. Matsumoto, H. Saito, and S. Ozawa, “3D reconstruction of skin surface from photometric stereo images with specular reflection and interreflection,” Electrical Engineering in Japan **129**, 51–58 (1999).

[79] A. Bashkatov and E. Genina, “Optical properties of human skin, subcutaneous and mucous tissues in the wavelength range from 400 to 2000 nm,” Journal of Physics **38**, 2543–2555 (2005).

[80] R. Anderson and J. Parrish, “The optics of human skin,” Journal of Investigative Dermatology **77**, 13–19 (1981).

[81] T. Chen, M. Goesele, and H.-P. Seidel, “Mesostructure from Specularity,” in “IEEE Computer Society Conference on Computer Vision and Pattern Recognition,” , vol. 2 (Ieee, 2006), vol. 2, pp. 1825–1832.

[82] M. Johnson, F. Cole, A. Raj, and E. Adelson, “Microgeometry capture using an elastomeric sensor,” ACM Transactions on Graphics p. 1 (2011).

[83] Y. Zhou, M. L. Smith, L. Smith, and R. Warr, “Combinatorial photometric stereo and its application in 3D modeling of melanoma,” Machine Vision and Applications **23**, 1029–1045 (2011).

[84] T. Malzbender and B. Wilburn, “Surface enhancement using real-time photometric stereo and reflectance transformation,” in “European Symposium on Rendering,” (2006), pp. 245–250.

[85] J. a. Paterson, D. Claus, and A. W. Fitzgibbon, “BRDF and geometry capture from extended inhomogeneous samples using flash photography,” Computer Graphics Forum **24**, 383–391 (2005).

[86] D. BARKER, “Skin thickness in the human,” Plastic and Reconstructive Surgery **7**, 115 (1951).

[87] Y. Lee and K. Hwang, “Skin thickness of Korean adults,” Surgical and radiologic anatomy **24**, 183–9 (2002).

[88] V. V. Barun, a. P. Ivanov, a. V. Volotovskaya, and V. S. Ulashchik, “Absorption spectra and light penetration depth of normal and pathologically altered human skin,” Journal of Applied Spectroscopy **74**, 430–439 (2007).

[89] A. Krishnaswamy and G. V. Baranoski, “A Biophysically-Based Spectral Model of Light Interaction with Human Skin,” Computer Graphics Forum **23**, 331–340 (2004).

[90] J. Federici, N. Guzelsu, H. Lim, G. Jannuzzi, T. Findley, H. Chaudhry, and A. Ritter, “Noninvasive light-reflection technique for measuring soft-tissue stretch,” Applied optics **38**, 6653–6660 (1999).

[91] K. Dana, “BRDF/BTF measurement device,” in “ICCV,” , vol. 2 (IEEE, 2001), vol. 2, pp. 460–466.

[92] K. Dana, B. Van Ginneken, S. Nayar, and J. Koenderink, “Reflectance and texture of real-world surfaces,” ACM Transactions on Graphics **18**, 1–34 (1999).

[93] S. R. Marschner, S. H. Westin, E. P. F. Lafortune, K. E. Torrance, and D. P.

Greenberg, “Image Based BRDF Measurement Including Human Skin,” in “Eurographics Workshop on Rendering,” (1999), pp. 131–144.

[94] E. Angelopoulou, “The reflectance spectrum of human skin,” Tech. rep., University of Pennsylvania (1999).

[95] B. Koch, “A multispectral bidirectional reflectance distribution function study of human skin for improved dismount detection,” Ph.D. thesis, Airforce Institue of Technology (2011).

[96] C. Chao, H. Tu, K. Chou, P. Chou, and F. Hsueh, “Crosstalk metrics and the characterization of 1.1um-pixel CIS,” in “International Image Sensor Workshop,” (2011), 5, pp. 3–6.

[97] B. K. Park, W. Choe, J. Lim, S. Lee, and C. Kim, “Color correction with edge preserving and minimal SNR decrease using multi-layer decomposition,” Proc. SPIE **8296** (2012).

[98] D. Pascale, “RGB Coordinates of the Macbeth color checker,” Tech. rep. (2006).

[99] P. Burns, “Analysis of image noise in multispectral color acquisition,” Ph.D. thesis, The Rochester Institute of Technology (1997).

[100] M. Newberry, “Increasing Precision and Accuracy in Photometric Measurements,” Precision CCD Photometry **189**, 74–82 (1999).

[101] J. Lagarde, C. Rouvrais, D. Black, S. Diridollou, and Y. Gall, “Skin topography measurement by interference fringe projection: a technical validation,” Skin Research and Technology **7**, 112–121 (2001).

[102] R. Bazin and J. L. Lévêque, “Longitudinal study of skin aging: from microrelief to wrinkles,” Skin research and technology **17**, 135–40 (2011).

[103] M. Setaro and A. Sparavigna, “Irregularity skin index (ISI): a tool to evaluate skin surface texture,” Skin research and technology **7**, 159–63 (2001).

[104] T. Fujimura, K. Haketa, M. Hotta, and T. Kitahara, “Global and systematic demonstration for the practical usage of a direct in vivo measurement system to evaluate wrinkles,” International journal of cosmetic science **29**, 423–436 (2007).

[105] F. Meyer, “Topographic distance and watershed lines,” Signal Processing **38**, 113–125 (1994).

[106] Y.-H. Choi, Y.-S. Tak, S. Rho, and E. Hwang, “Accurate Wrinkle Representation Scheme for Skin Age Estimation,” 2011 Fifth FTRA International Conference on Multimedia and Ubiquitous Engineering **1**, 226–231 (2011).

[107] B. Muralikrishnan, *Computational surface and roundness metrology* (2009).

[108] R. Frankot and R. Chellappa, "A method for enforcing integrability in shape from shading algorithms," IEEE Transactions on Pattern Analysis and Machine Intelligence **10**, 439–451 (1988).

[109] C. Yuan, J. Li, X. Yan, and Z. Peng, "The use of the fractal description to characterize engineering surfaces and wear particles," Wear **255**, 315–326 (2003).

[110] "http://161.112.232.32/softgauges/SP_Surf_Para.htm#Ra," .

[111] D. Nečas and P. Klapetek, "Gwyddion: an open-source software for SPM data analysis," Central European Journal of Physics **10**, 181–188 (2011).

[112] P. Besl and N. McKay, "A method for registration of 3-D shapes," IEEE Transactions on pattern analysis and machine intelligence **14**, 239–256 (1992).

[113] J. Dong and M. Chantler, "Estimating parameters of an illumination model for the synthesis of specular surface textures," in "Computer and Information Technology," (IEEE, 2004), pp. 716–721.

[114] Z. Liang, J. Dong, X. Dong, X. Hu, and J. Xu, “Relations between Surface Gradient Maps in Frequency Domain and Application in Diffuse Component Detection,” Global Congress on Intelligent Systems pp. 221–225 (2009).

[115] N. Umov, “Chromatische depolarisation durch lichtzerstreung,” Phys. Zeits **6**, 674–676 (1905).

[116] G. a. Atkinson and E. R. Hancock, “Recovery of surface orientation from diffuse polarization,” IEEE transactions on image processing **15**, 1653–64 (2006).

[117] G. Atkinson and E. Hancock, “Surface reconstruction using polarization and photometric stereo,” Computer Analysis of Images and Patterns pp. 466–473 (2007).

[118] A. Dutta, “Face Shape and Reflectance Acquisition using a Multispectral Light Stage,” Ph.D. thesis, University of York (2011).

[119] S. Ikehata, D. Wipf, Y. Matsushita, and K. Aizawa, “Robust photometric stereo using sparse regression,” IEEE Conference on Computer Vision and Pattern Recognition **1**, 318–325 (2012).

[120] C. Yu, Y. Seo, and S. Lee, “Photometric stereo from maximum feasible Lambertian reflections,” ECCV 2010 pp. 115–126 (2010).

[121] H.-s. Chung, “Efficient photometric stereo on glossy surfaces with wide specular lobes,” in “IEEE Conference on Computer Vision and Pattern Recognition,” (Ieee, 2008), pp. 1–8.

[122] A. Georghiades, “Incorporating the Torrance and Sparrow model of reflectance in uncalibrated photometric stereo,” in “ICCV,” (2003), Iccv, pp. 0–7.

[123] E. Zubko, G. Videen, Y. Shkuratov, K. Muinonen, and T. Yamamoto, “The Umov effect for single irregularly shaped particles with sizes comparable with wavelength,” Icarus **212**, 403–415 (2011).

[124] T. Weyrich, H. W. Jensen, M. Gross, W. Matusik, H. Pfister, B. Bickel, C. Donner, C. Tu, J. McAndless, J. Lee, and A. Ngan, “Analysis of human faces using a measurement-based skin reflectance model,” ACM Transactions on Graphics **25**, 1013 (2006).

Glossary

Anisotropic

A property of being directionally dependent.

Apocrine Sweat Glands

Glands producing thick secretions with little role in body temperature regulation.

Basement Membrane

A thin membranous layer of fibers that underlies epithelium and surrounds organs.

BRDF (Bidirectional Reflectance Distribution Function)

It's a function that describes how an incoming light is reflected by the object and is represented in units of steradian (sr^{-1}).

Collagen

A structural protein supporting major body organs.

Dermis

Middle layer of skin between epidermis and subcutaneous layer.

Dyspigmentation

A disorder of skin pigmentation.

Eccrine sweat glands

Sweat glands involved in cooling the body tempratures.

Ectoderm

Greek word meaning outside. Outermost germ cell layer in embryo.

Elastin

A structural protein that gives elasticity to structures.

Epidermis

Outermost layer of skin.

Horny cells

Cells making the outermost layer of skin also called as corneocytes.

ICP (Iterative Closest Point)

An algorithm for aligning two roughly aligned 3D surfaces such that the RMS between them is minimized.

keratinocytes

Cells residing in the basal layer of epidermis which differentiate to form other cell layers as they move upwards towards the upper most layer of epidermis.

Langerhan Cells

Antigen presenting cells that are a part of immune system.

Melanocytes

Melanin (black pigment) producing cells.

Mesoderm

Middle layer of three primary germ cell layers.

MERL (Mitsubishi Electric Research Laboratories)

Contains online database of skin reflectance data.

Mucopolysaccharides

Long chains of sugar molecules found in body. Also called as glycosaminoglycans.

Near Infrared

A wavelength of light just outside the visible range above the red part of the visible spectrum. More specifically it refers to a wavelength in the region of 850nm for the purposes of this thesis.

Photometric stereo

Invented by Woodham [56], photometric stereo is a method of estimating the surface orientation using multiple illuminations of an object from a single viewpoint.

Prickle Cell Layer

Also called as stratum spinosum (one of the layers of epidermis) made up of prickle cells(keratin producing cells).

RMS (Root Mean Squared)

Is a measure of the magnitude of variation between two quantities. The RMS error is used to quantify the difference between surface reconstructions in this thesis.

SEM (Scanning Electron Microscope)

It uses a high energy focused beam of electrons to scan a surface and acquires surface texture by analysing the electron-surface interactions.

SFS (Shape-from-Shading)

Refers to the technique of estimating the 3D shape of an object from a 2D image. Photometric stereo is a type of shape from shading where certain

associated ambiguities are removed (e.g. by separating texture from gradient) through multiple illumination sources.

Stratum Corneum

Outermost layer of skin made up of horny cells. Consists of 15 to 20 layers of horny cells.

List of Symbols

S_a	Arithmetic mean height calculated over the surface
S_p	Distance between highest point of the surface and mean line
S_{max}	Maximum distance between the highest and lowest point of the surface
S_z	Mean value of the distance between highest and lowest of the surface within five consecutively equally spaced sections
R_a	Arithmetic mean deviation of a profile
R_t	Total height of a profile
R_z	Maximum height of a profile
R_m	Maximum distance between the highest and lowest point of the profile
R_{ku}	Kurtosis (degree of peakedness) of the assessed profile
R_{sk}	Skewness of the assessed profile.
I	Reflected intensity of a point
E	Irradiance (incident power per unit area)
N	Surface normal vector

L	Light source direction
V	Viewing vector
R	Light Reflection vector
H	Halfway Vector is the vector that lies between the viewing and light vector
ρ	Surface albedo
k_d	Diffuse reflection coefficient
k_s	Specular reflection coefficient
θ_i	Zenith angle of incident light
θ_r	Zenith angle of reflected light
ϕ_i	Azimuth angle of incident light
ϕ_r	Azimuth angle of reflected light
ω_i	Direction of incident irradiance on the surface
ω_r	Reflected radiance
θ_s	Specular fall off angle. It is the angle between reflection vector and viewing vector
α	Variable that determines the size of specular reflection lobe
D	Microfacet distribution term used in the Torrance Sparrow model
F	Fresnel reflection
G	Geometric attenuation term used in the Torrance Sparrow model

η	Index of refraction
m	Root mean square slope of microfacets
σ_x	Variable that controls the width of lobe in x direction (Ward model)
σ_y	Controls the width of lobe in y direction (Ward model)
ρ_s	Specular reflection coefficient in Ward model
ρ_d	Diffuse reflection coefficient in Ward model
α_s	Constant used in the 3D gaussian filter equation and is equal to 0.4697
λ_{xc}	3D gaussian filter cutoff in x
λ_{yc}	3D gaussian filter cutoff in y
D_f	Fractal dimension
(c,r)	2D spatial frequency coordinates
$H(c,r)$	Fourier domain representation of surface height map
P	Degree of polarisation

Appendix A

Datasheets

Following are the datasheets of all the LEDs, Cameras and filters used.

A.1 LED Datasheet

Copyrighted Content
Contact author for details

Copyrighted Content
Contact author for details

Copyrighted Content
Contact author for details

Copyrighted Content
Contact author for details

Copyrighted Content
Contact author for details

Copyrighted Content
Contact author for details

Copyrighted Content
Contact author for details

Copyrighted Content
Contact author for details

Copyrighted Content
Contact author for details

Copyrighted Content
Contact author for details

Copyrighted Content
Contact author for details

Copyrighted Content
Contact author for details

A.2 Camera Datasheet

Copyrighted Content
Contact author for details

Copyrighted Content
Contact author for details

A.3 Camera Datasheet

Copyrighted Content
Contact author for details

Copyrighted Content
Contact author for details

Copyrighted Content
Contact author for details

A.4 Triband Filter Datasheet

Copyrighted Content
Contact author for details

Copyrighted Content
Contact author for details

Appendix B

Mathematical Derivations

B.1 Cross Product for Normal Vector Calculation

The normal vector n is given by the cross product of two non-parallel tangents lying on the facet as:

$$g_x = [\partial_x, 0, p\partial_x]^T \equiv [1, 0, p] \tag{B.1}$$
$$g_y = [0, \partial_y, q\partial_y]^T \equiv [0, 1, q] \tag{B.2}$$

By taking the cross product of these two vectors we can obtain the vector perpendicular to facet plane. Where the cross product of standard basis vectors i, j, k is given by:

$$i \times i = j \times j = k \times k = 0 \tag{B.3}$$

$$i \times j = k \tag{B.4}$$
$$j \times k = i \tag{B.5}$$
$$k \times i = j \tag{B.6}$$

$$j \times i = -k \tag{B.7}$$
$$k \times j = -i \tag{B.8}$$
$$i \times k = -j \tag{B.9}$$

$$g_x \times g_y = [1_i, 0_j, p_k] \times [0_i, 1_j, q_k] \tag{B.10}$$

$$\begin{aligned} g_x \times g_y = {} & 0(i \times i) + 1(i \times j) + q(i \times k) \\ & + 0(j \times i) + 0(j \times j) + 0(j \times k) \\ & + 0(k \times i) + p(k \times j) + pq(k \times k) \end{aligned}$$

$$g_x \times g_y = 0 + k + q(-j) + 0 + 0 + 0 + 0 + p(-i) + pq(0) \tag{B.11}$$

$$g_x \times g_y = k - qj - pi \tag{B.12}$$

$$g_x \times g_y = -pi - qj + k \tag{B.13}$$

or in matrix form it can be written as:

$$g_x \times g_y = [\text{-}p, \text{-}q, 1] \tag{B.14}$$

B.2 Constraint calculation for diffuse component

The constraint calculation was proposed by Liang and Dong in [113, 114].

Given a spatial surface height map given by $S(x,y)$:

$$Z = S(x,y) \tag{B.15}$$

At a given point on a surface $S(x,y)$ the gradients in x and y directions are given as:

$$\text{grad}(S(x,y)) = (p(x,y), q(x,y)) = [\frac{\partial z(x,y)}{\partial x}, \frac{\partial z(x,y)}{\partial y}] \tag{B.16}$$

By taking the Fourier transform ($\mathscr{F}$) of each pair of surface gradients $p(x,y)$ and $q(x,y)$ we get their corresponding expressions in frequency domain *P(c, r), Q(c, r)*.

$$\mathscr{F}(p(x,y)) = P(c,r) = icH(c,r) \tag{B.17}$$

$$\mathscr{F}(q(x,y)) = Q(c,r) = irH(c,r) \tag{B.18}$$

- Where $H(c,r)$ is the Fourier domain representation of the surface height map $S(x,y)$.
- (c,r) represents the 2D spatial frequency coordinate.
- where i is:

$$i = \sqrt{-1} \tag{B.19}$$

Dividing Eq. B.17 by B.18 we get.

$$rP(c,r) = cQ(c,r) \tag{B.20}$$

And the constraint was obtained by minimising the two sides of B.20

$$|rP(c,r) - cQ(c,r)| \tag{B.21}$$